



Contents lists available at ScienceDirect

International Journal of Mechanical Sciences

journal homepage: www.elsevier.com/locate/ijmecsci

Wrinkling as a mechanical instability in growing annular hyperelastic plates

Sumit Mehta^a, Gangadharan Raju^a, Prashant Saxena^{b,*}^a Department of Mechanical and Aerospace Engineering, Indian Institute of Technology, Hyderabad, India^b James Watt School of Engineering, University of Glasgow, Glasgow G12 8LT, UK

ARTICLE INFO

Keywords:

Growth
Plate theory
Bifurcation
Nonlinear elasticity

ABSTRACT

Growth-induced instabilities are ubiquitous in biological systems and lead to diverse morphologies in the form of wrinkling, folding, and creasing. The current work focusses on the mechanics behind growth-induced wrinkling instabilities in an incompressible annular hyperelastic plate. The governing differential equations for a two-dimensional plate system are derived using a variational principle with no a priori kinematic assumptions in the thickness direction. A linear bifurcation analysis is performed to investigate the stability behaviour of the growing hyperelastic annular plate by considering both axisymmetric and asymmetric perturbations. The resulting differential equations are then solved numerically using the compound matrix method to evaluate the critical growth factor that leads to wrinkling. The effect of boundary constraints, thickness, and radius ratio of the annular plate on the critical growth factor is studied. For most of the considered cases, an asymmetric bifurcation is the preferred mode of instability for an annular plate. Our results are useful to model the physics of wrinkling phenomena in growing planar soft tissues, swelling hydrogels, and pattern transition in two-dimensional films growing on an elastic substrate.

1. Introduction

The growth process typically involves a change of body mass and generation of residual stresses in an evolving system which induces large deformation that triggers the mechanical instabilities. These growth-induced instabilities lead to the formation of diverse patterns in the form of wrinkling, folding, creasing [1] that are critical to biological systems such as plants [2,3], tissues, and organs [4]. Moreover, certain anomalies in human biological systems like narrowing airways due to asthma [5], and malformation of the cerebral cortex [6] give rise to patterns that defines a new physiological function of the biological system. In addition, to avoid scar formation during surgeries, irregular wrinkles generated during cutaneous wound healing are studied [7,8]. Besides biological applications, pattern formation and their transition during growth and remodelling have been extensively studied from a purely mechanics aspect of view [9–14]. Instabilities in soft solids such as swollen hydrogels [15] and elastomers [16,17] can be tailored to create desired patterns and have found applications in the design of stretchable electronics [18], smart morphable surfaces in aerodynamics control [19], wearable communication devices [20], and shape-shifting structures [21]. Therefore, it is fundamentally important to understand the mechanics of growth that regulate the instabilities in soft growing bodies. To accomplish this, a consistent mathematical model based on the continuum mechanics framework is used for studying growth-induced instabilities in morpho-elastic structures [22,23].

To describe the kinematics of growth, the total deformation gradient is decomposed into a growth tensor and an elastic deformation tensor [24] ignoring the initial residual stress configuration [25,26]. The former tensor describes the local change in volume with the addition/subtraction of material as well as the deformation incompatibility due to non-uniform growth in the neighbourhood of a material point [27,28]. The elastic deformation tensor is required to ensure compatibility and this generally results in residual stresses that can trigger mechanical instabilities. Based on this principle, growth-induced instabilities have been extensively studied in soft biological tissues [1,9,29–33] as well as swelling hydrogels [34].

Numerous works employ a hyperelastic membrane model to study instabilities in thin soft tissues [35–37]. Jia et al. [38] studied the bifurcation behaviour of thin growing film on a cylindrical substrate. They showed that curvature delays the bifurcation point and requires a high magnitude of growth factor to induce the circumferential wrinkling instability on a curved surface. Recently, Wang et al. [39] developed a model to describe the nonlinear behaviour of hyperelastic curved shells under finite-strain. They explored the effect of curvature on the tunability of wrinkling and smoothing regimes, and the post-buckling evolution of a highly stretched soft shell. Above works show the interplay between growth and elasticity induces large deformation and one needs to adopt consistent plate or shell theories to capture the

* Corresponding author.

E-mail address: prashant.saxena@glasgow.ac.uk (P. Saxena).<https://doi.org/10.1016/j.ijmecsci.2022.107481>

Received 29 March 2022; Received in revised form 22 June 2022; Accepted 22 June 2022

Available online 28 June 2022

0020-7403/© 2022 The Author(s). Published by Elsevier Ltd. This is an open access article under the CC BY license (<http://creativecommons.org/licenses/by/4.0/>).

combined effect of bending and stretching deformation. Classical plate theories like Kirchhoff–Love, Föppl–von Kármán (FvK), and Mindlin–Reisner theory have been widely used to investigate the bifurcation behaviour of thin elastic structures [40–42], and liquid crystal elastomers [43]. Dervaux et al. [44] developed a FvK plate theory to investigate large deformation and growth-induced patterns in a thin hyperelastic plate. Efrati et al. [45] proposed the geometric theory for non-Euclidean thin plates to capture the large displacements in thin growing bodies where growth deformations are interpreted as the evolution metric. Based on this theory, Pezzulla et al. [46] studied the mechanics of thin growing bilayers by describing the geometry of mid surface with first and second fundamental form and Dias et al. [47] presented the inverse approach to investigate the growth (swelling) patterns of initially prescribed axisymmetric shapes. Jones and Mahadevan [48] developed the numerical framework to determine the optimal distribution of growth stresses by specifying the deformed target shape of the plate using FvK theory. Holmes [49] performed post-bifurcation analysis to investigate the instability phenomena in thin soft materials. Further, Mora and Boudaoud [50] experimentally and theoretically investigated the patterns arising from differential swelling of gels to mimic the behaviour of growth-induced deformation in biological tissues. However, these theories are based on a priori assumptions of displacement variation along the thickness of the plate and therefore have certain limitations. This has led to the development of a reduced 2-D plate theories with no a priori kinematic assumptions that are consistent with the 3-D elasticity theory.

Kienzler [51] proposed a consistent asymptotic plate theory based on linear elasticity which does not apply any kinematic assumptions and all the unknowns are treated as independent variables. Dai and Song [52] proposed a finite-strain plate theory for compressible hyperelastic materials based on the principle of minimisation of potential energy which can achieve term-wise consistency without any ad-hoc assumption for general loading conditions. Wang et al. [53] extended this approach to incompressible hyperelastic materials with an additional Lagrange multiplier to accommodate the incompressibility constraint. Wang et al. [54] derived a consistent finite-strain plate theory for growth-induced large deformation and studied the buckling and post-buckling behaviour of a thin rectangular hyperelastic plate subjected to axial growth. They also showed that the consistent theory reduces to the FvK theory in the limit of small plate thickness. Recently, the finite-strain asymptotic plate theory has been applied to study the plane strain problems of growth-induced deformation in single and multi-layered hyperelastic plates [55,56]. Wang et al. [57] studied the inverse approach of determining the inhomogeneous growth fields of target 3-D shapes by using stress-free [58] finite-strain theory for thin hyperelastic plates. Liu et al. [59] discussed the large elastic deformation in nematic liquid crystal elastomer and the authors of the present paper [60] investigated the bifurcation behaviour of circular hyperelastic plate under the influence of growth using finite-strain asymptotic plate theory.

Instability behaviour of highly deformable soft tissues is best understood by a bifurcation analysis of the corresponding system of partial differential equations (PDEs) [61]. Generally an analytical solution is not possible and numerical approaches based on the finite element method are appropriate [62,63]. Specialised finite element approaches have been employed to compute growth-induced deformation in soft materials while avoiding the volumetric locking arising from the assumption of incompressibility. Zheng et al. [64] developed the solid-shell based finite element model to investigate the growth deformation in incompressible thin-walled soft structures. Groh [65] developed the seven parameter quadrilateral shell element to avoid locking phenomena in shells and investigated the growth-induced instability in slender structures. Kadapa et al. [66] proposed the mixed displacement-pressure finite element formulation to study the compressible and incompressible deformation in growth problems. A virtue of the plate theory used in this paper, on the other hand, is that it works well with

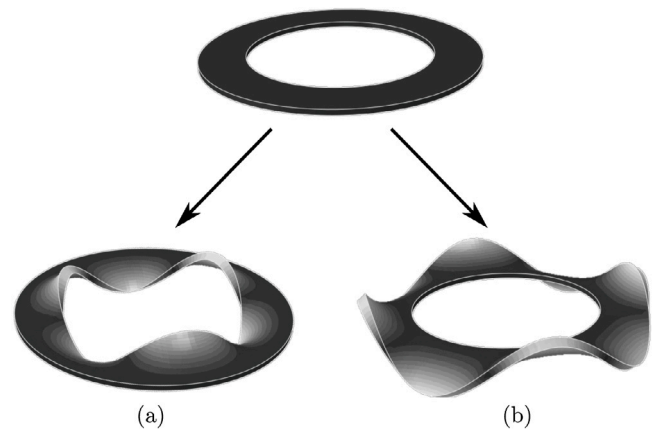


Fig. 1. Possible out-of-plane wrinkled configurations of a hyperelastic annular plate growing with in-plane growth function when subjected to different type of boundary conditions i.e., (a) constrained outer boundary and unconstrained inner boundary, and (b) constrained inner boundary and unconstrained outer boundary. The reference configuration (left) is a flat plate and the deformed configurations (right) are the buckled/wrinkled configuration. In each case, the unconstrained boundary exhibits wrinkles induced by growth.

both compressible and incompressible materials without imposing any kinematic assumptions. We provide quantitative comparisons obtained via our approach with existing computational results in the literature.

The current work investigates wrinkling phenomena in growing hyperelastic annular plates that are appropriate models for human tissues and plants [67,68] when subjected to different boundary constraints as shown in Fig. 1. For example, (a) wrinkling patterns around contracting skin wound subjected to constrained outer edge conditions [69, Figure 5] (b) wrinkle formation in a circular shaped leaf when the stiff inner part can be approximated by a clamped boundary condition. Note that we limit our discussion to only out of plane wrinkling instabilities and have not considered local instabilities like folding [70] or creasing [71–73]. In general, growing systems are more appropriately modelled by anisotropic and inhomogeneous (differential) growth laws that lead to diverse patterns [4,74] governing the final shape of the system. However, in this work, we assume an externally-driven homogeneous isotropic growth law to focus on the mechanics of growth in annular plate structures. The growth function is considered as a control parameter responsible for the change of shape [55,75] and the onset of instability. We also choose a neo-Hookean material model that allows us to model nonlinear deformation while still keeping the resulting equations relatively simple and retaining the key aspects of the mechanics of the system. We have applied the consistent finite-strain plate theory introduced by Wang et al. [54] to derive the governing differential equations (GDEs) for general loading conditions. Subsequently, we perform the stability analysis by perturbing the principal solution subjected to two different cases of boundary conditions. In the first case, the inner boundary of the annular plate is unconstrained and the outer boundary is constrained. For the second case, the inner boundary of the plate is constrained and the outer boundary is unconstrained. The resulting nonlinear ordinary differential equations (ODEs) are solved numerically to evaluate the critical value of growth parameter. For each case of boundary conditions, we investigate the type of perturbation namely, axisymmetric or asymmetric corresponding to stable bifurcation solution of the annular plate and also study the effect of plate thickness, radius ratio on the onset of instability.

1.1. Organisation of this manuscript

The remainder of this paper is organised as follows. In Section 2, a general formulation for a three-dimensional annular plate is established and then the same is reduced to a two-dimensional system

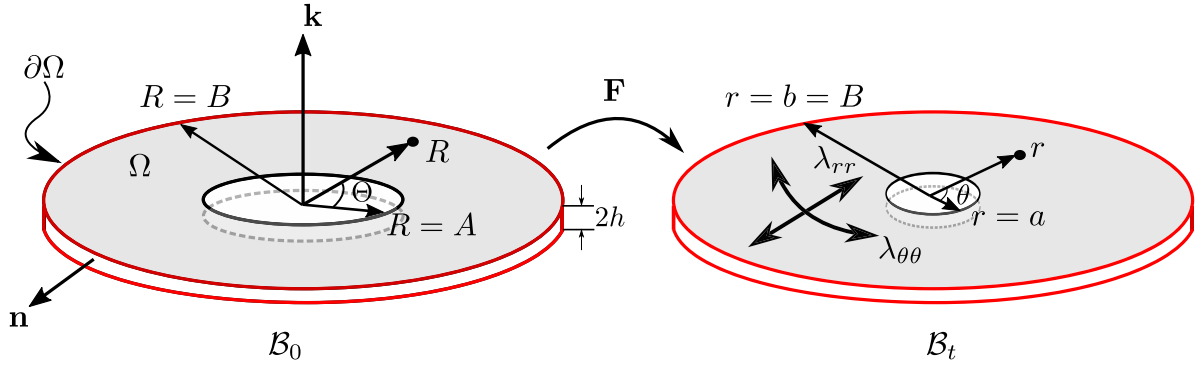


Fig. 2. A schematic of finite deformation of an annular plate due to growing region Ω with constrained outer boundary i.e., the outer radius is same in the reference, B_0 (left) and in the deformed, B_t (right) configuration. The region Ω is growing with a factor of λ_{rr} and $\lambda_{\theta\theta}$ in the radial and hoop directions, respectively.

by eliminating the dependence on the thickness variable using a series approximation. In Section 3, we discuss the principal solution associated with the growth-induced deformation in an incompressible neo-Hookean annular plate subjected to two different boundary conditions. We validate our 2-D plate framework by comparing the obtained numerical pre-buckling solution with the existing analytical solution of a circular ring later in this section. In Section 4, we derive the non-dimensional nonlinear ODEs associated with asymmetric as well as axisymmetric perturbations. Section 5 begins with a comparison of the current plate theory to FvK plate theory. Then, we apply the compound matrix method to solve the bifurcation problem and compare the bifurcation solutions associated with each type of perturbation and boundary conditions. At the end of this section, we provide the comparison of bifurcation solution obtained with this current plate theory with the existing solution obtained using finite element approach. Finally, we present our conclusion in Section 6. Supplementary mathematical derivations are provided in Appendix B.

1.2. Notation

Brackets: Two types of brackets are used. Round brackets $()$ are used to define the functions applied on parameters or variables. Square brackets $[\]$ are used to clarify the order of operations in an algebraic expression. Square brackets are also used for matrices and tensors. At some places we use the square bracket to define the functional.

Symbols: A variable typeset in a normal weight font represents a scalar. A lower-case bold weight font denotes a vector and bold weight upper-case denotes tensor or matrices. Tensor product of two vectors \mathbf{a} and \mathbf{b} is defined as $[\mathbf{a} \otimes \mathbf{b}]_{ij} = [\mathbf{a}]_i [\mathbf{b}]_j$. Tensor product of two second order tensors \mathbf{A} and \mathbf{B} is defined as either $[\mathbf{A} \otimes \mathbf{B}]_{ijkl} = [\mathbf{A}]_{ij} [\mathbf{B}]_{kl}$ or $[\mathbf{A} \boxtimes \mathbf{B}]_{ijkl} = [\mathbf{A}]_{ik} [\mathbf{B}]_{jl}$. Higher order tensors are written in bold calligraphic font with a superscript as $\mathcal{A}^{(i)}$, where superscript ' i ' tells that the function is differentiated $i+1$ times. For example, $\mathcal{A}^{(1)} = \frac{\partial f(\mathbf{A})}{\partial \mathbf{A} \partial \mathbf{A}}$ is a fourth order tensor. Operation of a fourth order tensor on a second order tensor is denoted as $[\mathcal{A}^{(1)} : \mathbf{A}]_{ij} = [\mathcal{A}^{(1)}]_{ijkl} [\mathbf{A}]_{kl}$. Inner product is defined as $\mathbf{a} \cdot \mathbf{b} = [\mathbf{a}]_i [\mathbf{b}]_i$ and $\mathbf{A} : \mathbf{B} = [\mathbf{A}]_{ij} [\mathbf{B}]_{ij}$. The symbol ∇ denotes the two-dimensional differentiation operator. We use the word 'Div' to denote divergence in three dimensions.

Functions: $\det(\mathbf{A})$ denote the determinant of a tensor \mathbf{A} . $\text{tr}(\mathbf{A})$ denote the trace of tensor \mathbf{A} . $\text{diag}(a, b, c)$ denotes a second order tensor with only diagonal entries a, b and c .

2. Governing equation with variational principle

Consider a thin annular plate with constant thickness ($2h$) occupying the region $\Omega \times [0, 2h]$ in the reference configuration $B_0 \in \mathcal{R}^3$ which then deforms to the current configuration $B_t \in \mathcal{R}^3$ as shown in Fig. 2. Coordinates of a point in the undeformed configuration are given by R, Θ, Z and in the deformed configuration by r, θ, z . Position

vector in B_0 is denoted as $\mathbf{X}(R, \Theta, Z)$ and denoted as $\mathbf{x}(r, \theta, z)$ in B_t . The inner and outer radii in the reference configuration are denoted as A and B , and the same in deformed configuration are denoted as a and b , respectively. Using the position vector \mathbf{X} and \mathbf{x} , the deformation gradient is expressed as $\mathbf{F} = \frac{\partial \mathbf{x}}{\partial \zeta} + \frac{\partial \mathbf{x}}{\partial Z} \otimes \mathbf{k}$, where $\zeta = R\mathbf{e}_R + \Theta\mathbf{e}_\Theta$ and \mathbf{k} is the unit normal to the surface Ω in the reference configuration. Following the multiplicative decomposition approach proposed by Rodriguez et al. [24], the total deformation gradient of a growing plate is decomposed as $\mathbf{F} = \mathbf{A}\mathbf{G}$ in $A \leq R \leq B$, where \mathbf{G} represents the growth tensor and \mathbf{A} represents the elastic deformation tensor. We also assume the material to be incompressible and therefore to follow the constraint $L(\mathbf{F}, \mathbf{G}) = L_0(\mathbf{F}\mathbf{G}^{-1}) = \det(\mathbf{A}) - 1 = 0$. The energy density (ϕ) per unit volume of the material is assumed as $\phi(\mathbf{F}, \mathbf{G}) = J_G \phi_0(\mathbf{F}\mathbf{G}^{-1})$, where $J_G = \det(\mathbf{G}) = \det(\mathbf{F})$ describes the local change in volume due to growth and $\phi_0(\mathbf{F}\mathbf{G}^{-1})$ is the elastic strain energy density. The internal potential energy functional (ψ) for the incompressible plate is

$$\psi[\mathbf{x}(\mathbf{X}), p(\mathbf{X})] = \int_{\Omega} \int_0^{2h} J_G \phi_0(\mathbf{F}\mathbf{G}^{-1}) dV - \int_{\Omega} \int_0^{2h} [J_G p(\mathbf{X}) L_0(\mathbf{F}\mathbf{G}^{-1})] dV, \quad (2.1)$$

where $p(\mathbf{X})$ is the Lagrange multiplier associated with the incompressibility constraint. We apply the principle of minimum potential energy and vanishing of the first variation with respect to \mathbf{x} and p of the above functional results in the GDEs with traction free boundary conditions

$$\text{Div } \mathbf{P} = \mathbf{0}, \quad \text{in } \Omega \times [0, 2h], \quad (2.2a)$$

$$\mathbf{P}\mathbf{k}|_{Z=0} = \mathbf{0}, \quad \mathbf{P}\mathbf{k}|_{Z=2h} = \mathbf{0}, \quad \text{on } \Omega, \quad (2.2b)$$

$$\mathbf{P}\mathbf{n}|_{R=A} = \mathbf{0}, \quad \mathbf{P}\mathbf{n}|_{R=B} = \mathbf{0}, \quad \text{on } \partial\Gamma \times [0, 2h], \quad (2.2c)$$

and the incompressibility constraint, i.e., $\det(\mathbf{A}) - 1 = 0$. Here, \mathbf{n} is the unit outward normal to the lateral boundary ($\partial\Gamma$) and $\mathbf{P} = J_G \left[\frac{\partial \phi_0}{\partial \mathbf{A}} - p \frac{\partial L_0}{\partial \mathbf{A}} \right] \mathbf{G}^{-T}$ in Ω is recognised as the first Piola Kirchhoff stress tensor.

2.1. Two-dimensional plate model

To obtain the 2-D formulation for the annular plate, we apply a series expansion of the unknown variables, \mathbf{x} and p about the bottom surface of plate ($Z = 0$) along the thickness direction following the approach by Wang et al. [54] and Wang et al. [55]

$$\mathbf{x}(\mathbf{X}) = \sum_{n=0}^3 \frac{Z^n}{n!} \mathbf{x}^{(n)}(\zeta) + O(Z^4), \quad \text{and} \quad p(\mathbf{X}) = \sum_{n=0}^3 \frac{Z^n}{n!} p^{(n)}(\zeta) + O(Z^4), \quad (2.3)$$

where we have used the notation $\mathbf{x}^{(n)} = \frac{\partial^n \mathbf{x}}{\partial Z^n}$ and $p^{(n)} = \frac{\partial^n p}{\partial Z^n}$. Using (2.3), we obtain a recursion relation for the deformation gradient as,

$\mathbf{F}^{(n)} = \nabla \mathbf{x}^{(n)} + \mathbf{x}^{(n+1)} \otimes \mathbf{k}$. Similarly, we expand the elastic tensor \mathbf{A} , and inverse transpose of growth tensor (\mathbf{G}^{-T}) to obtain the Piola Kirchhoff stress tensor \mathbf{P} (see (A.1)). Upon neglecting the body force and external traction, the equilibrium Eq. (2.2a) is given as the recursive relation

$$\nabla \cdot \mathbf{P}^{(n)} + \mathbf{P}^{(n+1)} \mathbf{k} = \mathbf{0}, \quad \text{for } n = 0, 1, 2. \quad (2.4)$$

Substituting $\mathbf{A} = \mathbf{F}\mathbf{G}^{-1}$ in the expression of Piola stress obtained as $\mathbf{P} = J_G \left[\frac{\partial \phi_0}{\partial \mathbf{A}} - p \frac{\partial L_0}{\partial \mathbf{A}} \right] \mathbf{G}^{-T}$ and making use of (2.4), we obtain the explicit expressions of $\mathbf{P}^{(0)}$, $\mathbf{P}^{(1)}$, and $\mathbf{P}^{(2)}$ which in component form ($[\mathbf{P}]_{ij} = P_{ij}$) are given as

$$P_{ij}^{(0)} = J_G \left[\mathcal{A}^{(0)} - p^{(0)} \mathcal{L}^{(0)} \right]_{ia} \bar{G}_{aj}^{(0)}, \quad (2.5a)$$

$$P_{ij}^{(1)} = J_G \left[\left[\mathcal{A}^{(1)} - p^{(0)} \mathcal{L}^{(1)} \right]_{iak\beta} A_{k\beta}^{(1)} - p^{(1)} \mathcal{L}_{ia}^{(0)} \right] \bar{G}_{aj}^{(0)} + \left[\mathcal{A}^{(0)} - p^{(0)} \mathcal{L}^{(0)} \right]_{ia} \bar{G}_{aj}^{(1)}, \quad (2.5b)$$

$$P_{ij}^{(2)} = J_G \left[\left[\mathcal{A}^{(1)}_{ik\alpha\beta} A_{\alpha\beta}^{(2)} + \left[\mathcal{A}^{(2)} - p^{(0)} \mathcal{L}^{(2)} \right]_{ik\alpha\beta mn} A_{\alpha\beta}^{(1)} A_{mn}^{(1)} - 2p^{(1)} \mathcal{L}_{ik\alpha\beta}^{(1)} A_{\alpha\beta}^{(1)} - p^{(0)} \mathcal{L}_{ik\alpha\beta}^{(1)} A_{\alpha\beta}^{(2)} - p^{(2)} \mathcal{L}_{ik}^{(0)} \right] \bar{G}_{kj}^{(0)} + \left[2\mathcal{A}_{ik\alpha\beta}^{(1)} A_{\alpha\beta}^{(1)} - 2p^{(0)} \mathcal{L}_{ik\alpha\beta}^{(1)} A_{\alpha\beta}^{(1)} - 2p^{(1)} \mathcal{L}_{ik}^{(0)} \right] \bar{G}_{kj}^{(1)} + \left[\mathcal{A}^{(0)} - p^{(0)} \mathcal{L}^{(0)} \right]_{ik} \bar{G}_{kj}^{(2)} \right], \quad (2.5c)$$

with $\mathcal{A}^{(i)}(\mathbf{A}^{(0)}) = \frac{\partial^{i+1} \phi_0(\mathbf{A})}{\partial \mathbf{A}^{i+1}} \Big|_{\mathbf{A}=\mathbf{A}^{(0)}}$ and $\mathcal{L}^{(i)}(\mathbf{A}^{(0)}) = \frac{\partial L_0(\mathbf{A})}{\partial \mathbf{A}^{i+1}} \Big|_{\mathbf{A}=\mathbf{A}^{(0)}}$. Further mathematical details of the above calculations are provided in the supplementary document. Eqs. (2.5b)–(2.5c) involve higher derivatives of \mathbf{A} which are obtained using the series expansion of \mathbf{F} and \mathbf{G}^{-T}

$$\begin{aligned} \mathbf{A}^{(0)} &= \mathbf{F}^{(0)} \bar{\mathbf{G}}^{(0)T}, \quad \mathbf{A}^{(1)} = \mathbf{F}^{(0)} \bar{\mathbf{G}}^{(1)T} + \mathbf{F}^{(1)} \bar{\mathbf{G}}^{(0)T}, \\ \mathbf{A}^{(2)} &= \mathbf{F}^{(0)} \bar{\mathbf{G}}^{(2)T} + 2\mathbf{F}^{(1)} \bar{\mathbf{G}}^{(1)T} + \mathbf{F}^{(2)} \bar{\mathbf{G}}^{(0)T}. \end{aligned} \quad (2.6)$$

The stress-free boundary conditions on the bottom and top surfaces of the annular plate are obtained from (2.2b) as

$$\mathbf{P}\mathbf{k}|_{Z=0} = \mathbf{P}^{(0)} \mathbf{k} = \mathbf{0}, \quad (2.7a)$$

$$\mathbf{P}\mathbf{k}|_{Z=2h} = \mathbf{P}^{(0)} \mathbf{k} + 2h\mathbf{P}^{(1)} \mathbf{k} + 2h^2\mathbf{P}^{(2)} \mathbf{k} + O(h^3) = \mathbf{0}, \quad (2.7b)$$

and the conditions associated with the incompressibility constraint upto second order are given by

$$\begin{aligned} L_0(\mathbf{A}^{(0)}) = 0, \quad \mathcal{L}^{(0)}[\mathbf{A}^{(1)}] = 0, \quad \mathcal{L}^{(0)}[\mathbf{A}^{(2)}] + \mathcal{L}^{(1)}[\mathbf{A}^{(1)}], \quad \mathbf{A}^{(1)} = 0, \\ \mathcal{L}^{(0)}[\mathbf{A}^{(3)}] + 3\mathcal{L}^{(1)}[\mathbf{A}^{(1)}, \mathbf{A}^{(2)}] + \mathcal{L}^{(2)}[\mathbf{A}^{(1)}, \mathbf{A}^{(1)}, \mathbf{A}^{(1)}] = 0, \end{aligned} \quad (2.8)$$

where $\mathcal{L}^{(0)}[\mathbf{A}^{(1)}] = \mathcal{L}^{(0)} : \mathbf{A}^{(1)} = \det(\mathbf{A})\mathbf{A}^{-T} : \mathbf{A}^{(1)}$. On subtracting the top (2.7b) and bottom (2.7a) traction conditions we obtain the 2-D plate GDE

$$\nabla \cdot \tilde{\mathbf{P}} = \mathbf{0}. \quad (2.9)$$

Here, $\tilde{\mathbf{P}} = \mathbf{P}^{(0)} + h\mathbf{P}^{(1)} + \frac{2}{3}h^2\mathbf{P}^{(2)}$ is the average stress obtained by simply taking the integration over the thickness of the plate, $\tilde{\mathbf{P}} = \frac{1}{2h} \int_0^{2h} \mathbf{P} dZ$. Using the series expansion approach, the equilibrium Eq. (2.9) is expressed as

$$\left. \begin{aligned} \nabla \cdot \mathbf{P}'_t + h\nabla \cdot \mathbf{P}'_t + \frac{2}{3}h^2\nabla \cdot \mathbf{P}'_t + O(h^3) = \mathbf{0}, \\ [\nabla \cdot \tilde{\mathbf{P}}] \cdot \mathbf{k} = \nabla \cdot [\mathbf{P}^{(0)T} \mathbf{k}] + h\nabla \cdot [\mathbf{P}^{(1)T} \mathbf{k}] + \frac{2}{3}h^2\nabla \cdot [\mathbf{P}^{(2)T} \mathbf{k}] + O(h^3) = 0, \end{aligned} \right\} \quad (2.10)$$

where the subscript 't' represents the in-plane (or tangential) component of a vector or tensor. Eq. (2.10) is then reduced to a refined plate

equation [76,77] by neglecting the contribution of $\mathbf{P}^{(2)}$, but keeping terms of $O(h^2)$ that correspond to the bending energy of the plate

$$\nabla \cdot \mathbf{P}'_t + h\nabla \cdot \mathbf{P}'_t = \mathbf{0}, \quad (2.11a)$$

$$\nabla \cdot [\mathbf{P}^{(0)T} \mathbf{k} - \mathbf{P}^{(0)} \mathbf{k}] + h \left[\nabla \cdot [\mathbf{P}^{(1)T} \mathbf{k} - \mathbf{P}^{(1)} \mathbf{k}] \right] + \frac{1}{3}h^2\nabla \cdot [\nabla \cdot \mathbf{P}'_t] = 0, \quad (2.11b)$$

The explicit expressions of unknown variables $\mathbf{x}^{(2)}$, $p^{(1)}$ and $\mathbf{x}^{(3)}$, $p^{(2)}$ in terms of $\mathbf{x}^{(0)}$, $\mathbf{x}^{(1)}$ and $p^{(0)}$ which result in a closed form system are provided in our previous work [60]. One advantage of this plate theory is that if we neglect the bending term in (2.10), the plate system is reduced to a membrane system. By solving the annular plate system (ignoring $O(h)$ and $O(h^2)$ terms in (2.10) or (2.11)) and applying an incompressible Varga hyperelastic material model, we recover the membrane equation obtained by Swain and Gupta [36].

3. Growth-induced deformation in annular plates

In this section, we discuss the deformation of an annular plate undergoing isotropic growth i.e., plate growing with equivalent constant growth factor (λ) in the radial and circumferential directions. The growth tensor \mathbf{G} then takes the form $\text{diag}(\lambda_{rr}, \lambda_{\theta\theta}, 1)$ where $\lambda_{rr} = \lambda_{\theta\theta} = \lambda$. To simplify the calculation, the plate is assumed to be made up of an incompressible neo-Hookean material with elastic strain-energy function $\phi(\mathbf{F}, \mathbf{G}) = J_G \phi_0(\mathbf{A}) = J_G C_0 [I_1 - 3]$, where $I_1 = \text{tr}(\mathbf{A}^T \mathbf{A})$ and $2C_0$ is the ground state shear modulus. Using (2.3), the series approximation of unknown variables about the bottom surface in the cylindrical coordinate system is given as

$$\begin{aligned} r(R, Z) &= \sum_{n=0}^{n=3} \frac{Z^n}{n!} r^{(n)}(R) + O(Z^4), & \theta(R, Z) &= \sum_{n=0}^{n=3} \frac{Z^n}{n!} \theta^{(n)}(R) + O(Z^4), \\ z(R, Z) &= \sum_{n=0}^{n=3} \frac{Z^n}{n!} z^{(n)}(R) + O(Z^4), & p(R, Z) &= \sum_{n=0}^{n=3} \frac{Z^n}{n!} p^{(n)}(R) + O(Z^4), \end{aligned} \quad (3.1)$$

where $(\cdot)^n = \frac{\partial^n (\cdot)}{\partial Z^n}$. The isotropic growth field with (3.1) results in

$$\begin{aligned} [\bar{\mathbf{G}}^{(0)}] &= \begin{bmatrix} \frac{1}{\lambda} & 0 & 0 \\ 0 & \frac{1}{\lambda} & 0 \\ 0 & 0 & 1 \end{bmatrix}, & [\mathbf{F}^{(0)}] &= \begin{bmatrix} \frac{\partial r^{(0)}}{\partial R} & \frac{1}{R} \frac{\partial r^{(0)}}{\partial \theta} & r^{(1)} \\ r^{(0)} \frac{\partial \theta^{(0)}}{\partial R} & \frac{r^{(0)}}{R} \frac{\partial \theta^{(0)}}{\partial \theta} & r^{(0)} \theta^{(1)} \\ \frac{\partial z^{(0)}}{\partial R} & \frac{1}{R} \frac{\partial z^{(0)}}{\partial \theta} & z^{(1)} \end{bmatrix}, \\ J_G = \det(\mathbf{G}) &= \lambda^2, \end{aligned} \quad (3.2)$$

where $\bar{\mathbf{G}}^{(0)}$ and $\mathbf{F}^{(0)}$ are the first terms in the expansion of \mathbf{G}^{-T} and \mathbf{F} , respectively. Explicit expressions for the unknown variables can be derived as

$$p^{(0)} = \frac{2C_0 \lambda^4}{|\nabla \mathbf{x}^{(0)*}|^2}, \quad r^{(1)} = \frac{p^{(0)} \Delta x_{11}}{2C_0 \lambda^2}, \quad \theta^{(1)} = \frac{p^{(0)} \Delta x_{22}}{2C_0 \lambda^2 r^{(0)}}, \quad z^{(1)} = \frac{p^{(0)} \Delta x_{33}}{2C_0 \lambda^2}. \quad (3.3)$$

Equations associated with the derivation of (3.3) and the terms corresponding to higher orders of $\bar{\mathbf{G}}$, \mathbf{F} are detailed in Appendix A.

3.1. Pre-buckling solution

The principal or pre-buckling axisymmetric solution is given by

$$r^{(0)}(R) = r(R), \quad \theta^{(0)} = \theta, \quad z^{(0)}(R) = C_Z, \quad (3.4)$$

where C_Z is a constant function. Upon substituting the principal solution (3.4) in the plate Eq. (2.11), we obtain a fourth order equation in $r^{(0)}$. This is transformed to four first order ODEs of the form

$$\mathbf{D}\mathbf{y}' = \mathbf{q}, \quad (3.5)$$

where a prime denotes derivative with respect to R , $\mathbf{D} = \text{diag}(1, 1, 1, D_1)$, $\mathbf{y}' = [r^{(0)'} \ r^{(0)''} \ r^{(0)'''} \ r^{(0)iv}]^T = [y'_1 \ y'_2 \ y'_3 \ y'_4]^T$, $\mathbf{q} = [y_2 \ y_3 \ y_4 \ D_2]^T$, and D_1 and D_2 are given as

$$D_1 = 2\rho_1^2 \rho_2^2 \rho_3^2 \bar{h}^2 \lambda^6 \left[4\rho_2^2 \lambda^6 + \rho_1^2 \rho_2^4 \right],$$

$$D_2 = 80 \bar{h}^2 \lambda^{12} \rho^8 \rho_1^3 \rho_2 \rho_3 \rho_4 - 72 \bar{h}^2 \lambda^{12} \rho^8 \rho_1^3 \rho_3^3 + 24 \bar{h}^2 \lambda^{12} \rho^8 \rho_1^2 \rho_2^3 \rho_4 + 64 \bar{h}^2 \lambda^{12} \rho^8 \rho_1^2 \rho_2^2 \rho_3^2 + 82 \bar{h}^2 \lambda^{12} \rho^8 \rho_1 \rho_2^4 \rho_3 - 6 \bar{h}^2 \lambda^{12} \rho^8 \rho_2^6 - 32 \bar{h}^2 \lambda^{12} \rho^7 \rho_1^3 \rho_2^2 \rho_4 - 24 \bar{h}^2 \lambda^{12} \rho^7 \rho_1^3 \rho_2 \rho_3^2 - 200 \bar{h}^2 \lambda^{12} \rho^7 \rho_1^2 \rho_2^3 \rho_3 - 82 \bar{h}^2 \lambda^{12} \rho^7 \rho_1 \rho_2^5 + 144 \bar{h}^2 \lambda^{12} \rho^6 \rho_1^3 \rho_2^2 \rho_3 + 136 \bar{h}^2 \lambda^{12} \rho^6 \rho_1^2 \rho_2^4 - 24 \bar{h}^2 \lambda^6 \rho^6 \rho_1^5 \rho_2^5 \rho_3 \rho_4 + 80 \bar{h}^2 \lambda^6 \rho^6 \rho_1^5 \rho_2^4 \rho_3^3 - 8 \bar{h}^2 \lambda^6 \rho^6 \rho_1^4 \rho_2^7 \rho_4 + 86 \bar{h}^2 \lambda^6 \rho^6 \rho_1^4 \rho_2^6 \rho_3^2 + 57 \bar{h}^2 \lambda^6 \rho^6 \rho_1^3 \rho_2^8 \rho_3 + 20 \bar{h}^2 \lambda^6 \rho^6 \rho_1^2 \rho_2^{10} + 9 \lambda^8 \rho^6 \rho_1^5 \rho_2^6 \rho_3 + 9 \lambda^8 \rho^6 \rho_1^4 \rho_2^8 - 48 \bar{h}^2 \lambda^{12} \rho^5 \rho_1^3 \rho_2^3 - 4 \bar{h}^2 \lambda^6 \rho^5 \rho_1^5 \rho_2^6 \rho_4 - 56 \bar{h}^2 \lambda^6 \rho^5 \rho_1^5 \rho_2^5 \rho_3^2 - 36 \bar{h}^2 \lambda^6 \rho^5 \rho_1^4 \rho_2^7 \rho_3 + 9 \bar{h}^2 \lambda^6 \rho^5 \rho_1^3 \rho_2^9 - 9 \lambda^8 \rho^5 \rho_1^5 \rho_2^2 + 12 \bar{h}^2 \lambda^6 \rho^4 \rho_1^6 \rho_2^5 \rho_4 - 60 \bar{h}^2 \lambda^6 \rho^4 \rho_1^6 \rho_2^4 \rho_3^2 - 104 \bar{h}^2 \lambda^6 \rho^4 \rho_1^5 \rho_2^6 \rho_3 - 93 \bar{h}^2 \lambda^6 \rho^4 \rho_1^4 \rho_2^8 + 3 \lambda^2 \rho^4 \rho_1^7 \rho_2^{10} \rho_3 + 92 \bar{h}^2 \lambda^6 \rho^3 \rho_1^6 \rho_2^5 \rho_3 + 64 \bar{h}^2 \lambda^6 \rho^3 \rho_1^5 \rho_2^7 + 3 \lambda^2 \rho^3 \rho_1^7 \rho_2^{11} + \bar{h}^2 \rho^2 \rho_1^7 \rho_2^{10} \rho_3 - 3 \lambda^2 \rho^2 \rho_1^8 \rho_2^{10} + \bar{h}^2 \rho \rho_1^7 \rho_2^{11} - \rho_1^8 \rho_2^{10} \bar{h}^2.$$

While deriving the above, we have used the dimensionless quantities

$$\rho = \frac{R}{B}, \quad \rho_1 = \frac{r^{(0)}}{B}, \quad \rho_2 = r^{(0)'}, \quad \rho_3 = r^{(0)''} B, \quad \rho_4 = r^{(0)'''} B^2, \quad \text{and}$$

$$\bar{h} = \frac{h}{B}. \tag{3.6}$$

The principal solution for $\lambda > 1$ allows the contraction of inner radius and expansion of outer radius of the plate which are investigated for two different boundary conditions. In the first boundary condition, we consider the inner boundary of the plate to be unconstrained or free to contract due to growth ($\lambda > 1$) and the outer boundary is constrained (IFOC¹). This condition is inspired from the behaviour of soft biological tissue such as skin where the wounded skin grows to close a wound [36,78]. The second boundary condition models a constrained inner edge and unconstrained outer edge (ICOF²) of a plate where only the outer edge is allowed to deform during growth process. This condition is akin to the deformation of plants and soft polymeric material such as swollen gels [50,79].

3.1.1. Case 1: Constrained outer boundary and unconstrained inner boundary

If the inner edge (at $\rho = A/B = A^*$) of the plate is free to contract or expand then the radial stress at inner edge on bottom and top surface is $P_{Rr}|_{Z=0} = P_{Rr}|_{Z=2h} = 0$ (which corresponds to $P_{Rr}^{(0)} = P_{Rr}^{(2)} = 0$ using (2.10)) and can further be rewritten in terms of dimensionless variables as

$$\lambda \left[\frac{2\rho_1}{\lambda} - \frac{2\lambda^5 A^{*2}}{\rho_1^2 \rho_2^3} \right] = 0, \tag{3.7a}$$

$$8\rho_2^2 A^{*5} \lambda^6 \rho_3 + 4\rho_2 \rho_1 \rho_4 A^{*5} \lambda^6 - 4\rho_3^2 \rho_1 A^{*5} \lambda^6 - 8\rho_2^3 A^{*4} \lambda^6 - 4\rho_2 \rho_1 \rho_3 A^{*4} \lambda^6 + 2\rho_2^8 \rho_1 A^{*3} + 7\rho_2^6 \rho_1^2 A^{*3} \rho_3 + \rho_2^5 \rho_1^3 \rho_4 A^{*3} + 8\rho_1^4 \rho_1^3 \rho_3^2 A^{*3} + 8\rho_2^2 \rho_1 A^{*3} \lambda^6$$

¹ IFOC — Inner boundary of the plate is unconstrained (free) and outer boundary of the plate is constrained.

² ICOF — Inner boundary of the plate is constrained and the outer boundary of the plate is free.

$$+ 3\rho_2^7 \rho_1^2 A^{*2} - \rho_2^5 \rho_1^3 \rho_3 A^{*2} - 15\rho_2^6 \rho_1^3 A^{*2} - 6\rho_2^4 \rho_1^4 \rho_3 A^{*2} + 10\rho_2^5 \rho_1^4 = 0. \tag{3.7b}$$

If the outer edge of the plate is constrained then the displacement of bottom and top surface at $\rho = 1$ is 0 i.e., $r^{(0)}(B) = B$, and $r^{(0)} + (2h)r^{(1)} + 2h^2 r^{(2)} = B$ and is given by

$$\rho_1(1) = 1, \tag{3.8a}$$

$$r^{(2)}(1) = -2\rho_2^2 \lambda^6 - 2\rho_1 \rho_3 \lambda^6 + 2\rho_2 \rho_1 \lambda^6 - \rho_2^4 \rho_1^3 \rho_3 - \rho_2^5 \rho_1^3 + \rho_2^4 \rho_1^4 = 0. \tag{3.8b}$$

3.1.2. Case 2: Constrained inner boundary and unconstrained outer boundary

If the inner edge of the plate is constrained then the displacement of bottom and top surface at the inner edge ($\rho|_{A^*} = 0$) is

$$r^{(0)}(A^*) = A^* \rightarrow \rho_1(A^*) = A^*, \tag{3.9a}$$

$$r^{(2)}(A^*) = -2\rho_2^2 A^{*4} \lambda^6 - 2\rho_1 \rho_3 A^{*4} \lambda^6 + 2\rho_2 \rho_1 A^{*3} \lambda^6 - \rho_2^4 \rho_1^3 \rho_3 A^{*2} - \rho_2^5 \rho_1^3 A^{*2} + \rho_2^4 \rho_1^4 = 0. \tag{3.9b}$$

If the outer edge is unconstrained, the radial stress $P_{Rr}^{(0)} = P_{Rr}^{(2)} = 0$ at $\rho = 1$ is expressed as

$$\lambda \left[\frac{2\rho_1}{\lambda} - \frac{2\lambda^5}{\rho_1^2 \rho_2^3} \right] = 0, \tag{3.10a}$$

$$8\rho_2^2 \lambda^6 \rho_3 + 4\rho_2 \rho_1 \rho_4 \lambda^6 - 4\rho_3^2 \rho_1 \lambda^6 - 8\rho_2^3 \lambda^6 - 4\rho_2 \rho_1 \rho_3 \lambda^6 + 2\rho_2^8 \rho_1 + 7\rho_2^6 \rho_1^2 \rho_3 + \rho_2^5 \rho_1^3 \rho_4 + 8\rho_1^4 \rho_1^3 \rho_3^2 + 8\rho_2^2 \rho_1 \lambda^6 + 3\rho_2^7 \rho_1^2 - \rho_2^5 \rho_1^3 \rho_3 - 15\rho_2^6 \rho_1^3 - 6\rho_2^4 \rho_1^4 \rho_3 + 10\rho_2^5 \rho_1^4 = 0. \tag{3.10b}$$

3.1.3. Numerical pre-buckling solution

In this section, we discuss the deformation associated with the principal solution (3.4) for both the boundary conditions. In the first case (IFOC), we numerically solve the system of ODEs (3.5) subjected to the boundary conditions (3.7) and (3.8). The numerical solutions for primary in-plane deformation of an annulus plate for different radius ratios $B/A = 1.1, 1.5, 2$ (see Fig. 3) are obtained using the `bvp4c` solver available in Matlab. The dependence of deformed inner radius (a/A) on the growth parameter ($\lambda > 1$) for a plate of thickness $\bar{h} = 0.03$ is presented in Fig. 3a. During growth, the inner boundary of the annular plate contracts resulting in a decrease of the inner radius ($a < A$). The plate with a high radius ratio $B/A = 2$ shows more contraction even for a smaller value of λ compared to the other ratios. The numerical pre-buckling solution for the second case (ICOF) is obtained by solving the system of ODEs (3.5) subjected to the boundary conditions (3.9) and (3.10). In this case, we have shown the variation of the deformed outer radius (b/B) with growth factor λ in Fig. 3b. The outer edge of the plate expands as λ increases and plates with higher radius ratio show more expansion in comparison to plates with smaller radius ratio.

3.2. Constrained growth of a circular ring

To validate the 2-D plate framework, we compare the pre-buckling solution of an isotropically growing thin annular plate with the analytical solution of an incompressible neo-Hookean circular ring growing with planar constant growth i.e., $\lambda_{rr} = \lambda_{\theta\theta} = 1.35$ provided by [80, Figure 9]. The ring is subjected to (i) outer constrained boundary (similar to IFOC in this work), and (ii) inner constrained boundary (similar to ICOF) boundary conditions. The stress distribution curves for (i), and (ii) boundary conditions are plotted in Figs. 4a, and 4b, respectively. A numerical solution of the incompressible circular ring with same boundary condition using solid-shell based finite element approach subjected to identical isotropic growth function is also given by Zheng et al. [64]. Both the analytical and numerical solution are in good agreement with each other. To test the accuracy of current plate theory, we numerically solved (3.5) subjected to both IFOC

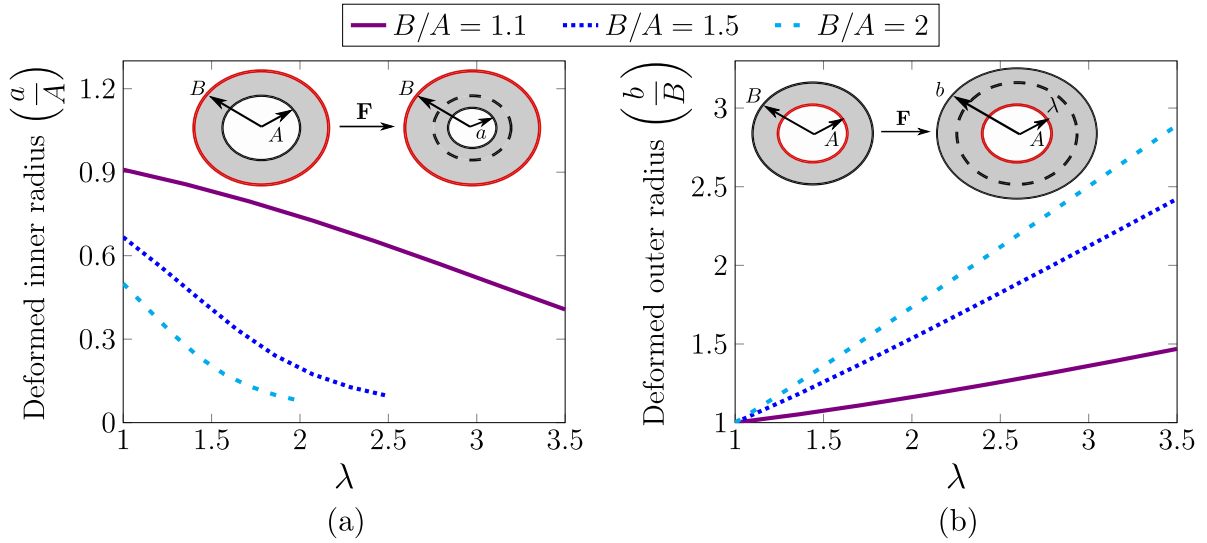


Fig. 3. (a) Dependence of the deformed inner radius (a/A) on growth factor λ at $\bar{h} = 0.03$ when outer edge of the plate is constrained and inner edge is unconstrained (IFOC), and (b) Dependence of deformed outer radius (b/B) on growth factor λ at $\bar{h} = 0.03$ when the inner edge of the plate is constrained and the outer edge is unconstrained (ICOF). In the first IFOC case, the inner boundary of the plate contracts and in the second ICOF case the outer unconstrained boundary expands on the application of λ . The deformed radius for both the cases is plotted for three different values of radius ratio that are $B/A = 1.1, 1.5,$ and 2 .

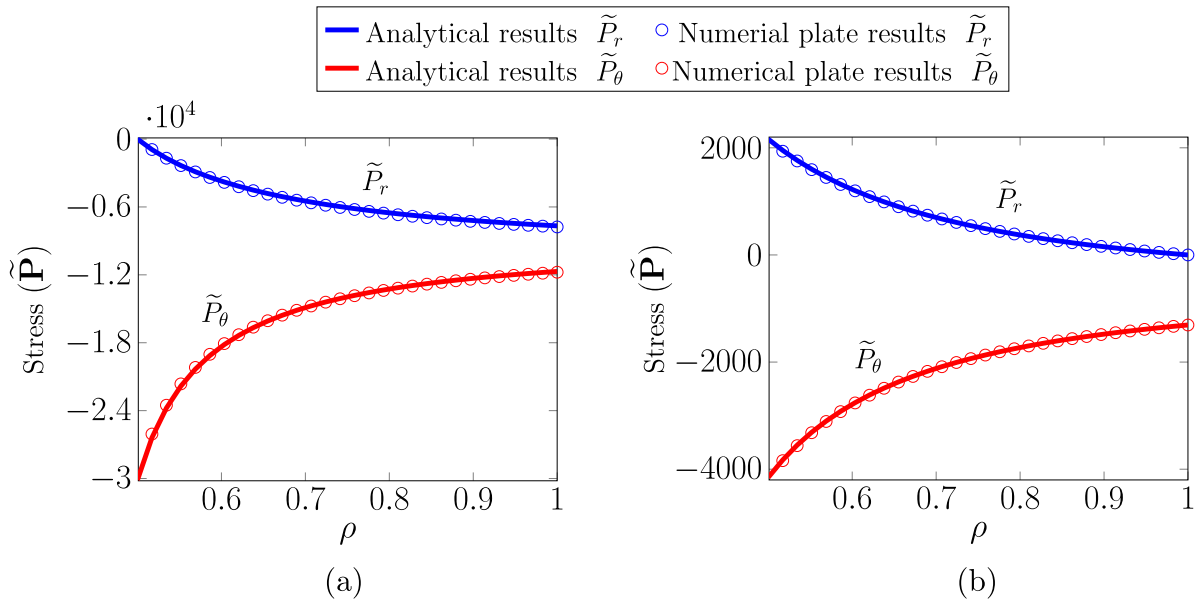


Fig. 4. Comparison of stress distribution obtained using current plate theory with the analytical results for a circular ring [80] for the both (a) IFOC, and (b) ICOF boundary conditions. The Piola Kirchhoff stress (both radial \tilde{P}_r and circumferential \tilde{P}_θ stress) are plotted against the normalised radius ρ . The radial and circumferential stress distribution curves are shown by blue and red colour lines, respectively. Numerical results of the current model are in perfect agreement with the analytical results.

((3.7)–(3.8)) and ICOF ((3.9)–(3.10)) boundary conditions using same parameters as $B/A = 2$, plate thickness, $2h = 0.001 \rightarrow 2\bar{h} = 0.0005$, growth stretch $\lambda = 1.35$ and ground state shear modulus $2C_0 = 4000$ by using the `bvp4c` solver in Matlab. The comparison of current numerical results with the existing analytical results are in good agreement. As shown in Fig. 4, numerical results obtained using the current theory are in agreement with the analytical results of Liu et al. [80] and numerical results of Zheng et al. [64].

4. Linear bifurcation analysis

We derive the PDEs for the onset of buckling in an isotropically growing annular plate. We seek a bifurcation solution close to the primary solution by using three different types of perturbations: (a) asymmetric perturbation along radial, circumferential and thickness

directions (i.e, r, θ, z coordinates), (b) axisymmetric perturbation along radial and thickness directions (i.e, r, z coordinates), and (c) asymmetric perturbation along circumferential and thickness directions (i.e, θ, z coordinates).

4.1. Perturbation along radial, circumferential and thickness direction

Consider the following small asymmetric perturbations to the pre-buckling solution (3.4) scaled by a parameter $0 < \epsilon \ll 1$

$$\begin{aligned} r^{(0)}(R, \Theta) &= r(R) + \epsilon \Delta U(R) \cos(m\Theta), \\ \theta^{(0)}(R, \Theta) &= \Theta + \epsilon \Delta V(R) \sin(m\Theta), \\ z^{(0)}(R, \Theta) &= z_z + \epsilon \Delta W(R) \cos(m\Theta), \end{aligned} \tag{4.1}$$

where $m = 1, 2, 3, \dots$ represents the wave number in the circumferential direction and C_z is a constant that models rigid motion of the plate. Upon substituting (4.1) in the plate governing Eq. (2.11), we obtain ODEs in terms of dimensionless displacement functions U, V and W as

$$a_1 U'' + a_2 U' + a_3 U + a_4 V' + a_5 V + a_6 W'''' + a_7 W'' + a_8 W' + a_9 W = 0, \quad (4.2a)$$

$$b_1 V'' + b_2 V' + b_3 V + b_4 U' + b_5 U + b_6 W'' + b_7 W' + b_8 W = 0, \quad (4.2b)$$

$$c_1 W'' + c_2 W' + c_3 W + c_4 U'' + c_5 U' + c_6 U + c_7 U + c_8 V'' + c_9 V' + c_{10} V + c_{11} W^{iv} + c_{12} W'' + c_{13} W'' + c_{14} W' + c_{15} W = 0, \quad (4.2c)$$

where $U = \Delta U/B$, $V = \Delta V/B$, and $W = \Delta W/B$. Eqs. (4.2a)–(4.2c) are rewritten into a system of first order differential equations by substituting $[y_1, y_2, \dots, y_8] = [U, U', V, V', W, W', W'', W''']$ resulting in

$$\mathbf{H}\mathbf{Y}' = \mathbf{g}. \quad (4.3)$$

Here, $\mathbf{H} = \text{diag}(1, a_1, 1, b_1, 1, 1, 1, c_{11})$ is an 8×8 matrix, and $\mathbf{Y}' = [y_1', y_2', y_3', y_4', y_5', y_6', y_7', y_8']^T$, and $\mathbf{g} = [y_1, y_2, y_3, y_4, y_5, y_6, y_7, y_8]^T$ are 8×1 column vectors. The coefficients in (4.2a)–(4.2c) are detailed in the supplementary document. The displacement boundary conditions for the IFOC case are

$$U'(A^*) = V(A^*) = W''(A^*) = W''''(A^*) = 0, \quad (4.4a)$$

$$U(1) = V(1) = W(1) = W'(1) = 0, \quad (4.4b)$$

and for the ICOF case are

$$U(A^*) = V(A^*) = W(A^*) = W'(A^*) = 0, \quad (4.5a)$$

$$U'(1) = V(1) = W''(1) = W''''(1) = 0. \quad (4.5b)$$

Here, Eqs. (4.4a) (respectively, (4.5b)) correspond to unconstrained inner edge (respectively, outer edge) of annular plate which allows contraction (respectively, expansion) and no restriction of bending moment ($W'' = 0$) and transverse shear ($W''' = 0$). Eqs. (4.4b) and (4.5a) correspond to clamped (constrained) outer and inner edges of the plate, respectively.

4.1.1. Perturbation along radial and thickness direction

In this case, the linear bifurcation analysis is performed by perturbing the principal solution (3.4) axisymmetrically with a small parameter $0 < \epsilon \ll 1$ by using the following ansatz

$$r^{(0)}(R, \Theta) = r(R) + \epsilon \Delta U(R) \cos(m\Theta), \quad \theta^{(0)} = \Theta, \\ z^{(0)}(R, \Theta) = C_z + \epsilon \Delta W(R) \cos(m\Theta), \quad (4.6)$$

where ' m ' is again an integer representing the wave number in the circumferential direction. On substituting (4.6) in the plate governing Eq. (2.11), we obtain ODEs in terms of the dimensionless displacement functions U and W which one can simply obtain by setting the coefficients $a_4 = a_5 = 0$ in (4.2a) and $c_8 = c_9 = c_{10} = 0$ in (4.2c). The system (4.2) is now reduced to two ODEs which is further simplified into six first-order linear differential equations of the form

$$\mathbf{B}\mathbf{m}' = \mathbf{m}, \quad (4.7)$$

where $\mathbf{m} = [U, U', W, W', W'', W''']$ and $\mathbf{B} = \text{diag}(1, a_1, 1, 1, 1, c_{11})$. The IFOC boundary condition is given as

$$U'(A^*) = W''(A^*) = W''''(A^*) = 0, \quad \text{and} \quad U(1) = W(1) = W'(1) = 0, \quad (4.8)$$

and the ICOF condition associated with this type of perturbation yields

$$U(A^*) = W(A^*) = W'(A^*) = 0, \quad \text{and} \quad U'(1) = W''(1) = W''''(1) = 0. \quad (4.9)$$

4.1.2. Perturbation along circumferential and thickness direction

In this case, the bifurcation solution is obtained by applying an asymmetric perturbation to the principal solution along circumferential and thickness directions using the following ansatz

$$r^{(0)}(R) = r(R), \quad \theta^{(0)}(R, \Theta) = \Theta + \epsilon \Delta V(R) \sin(m\Theta), \quad \text{and} \\ z^{(0)}(R, \Theta) = C_z + \epsilon \Delta W(R) \cos(m\Theta), \quad (4.10)$$

where $m = 1, 2, 3, \dots$ represents the circumferential wave number. In this type of perturbation, the incremental elastic strain is dependent on the Θ - Z coordinates. Thus, the incremental ODEs are obtained in terms of dimensionless displacement functions V and W by substituting (4.10) in (2.11) or we can obtain these ODEs by setting the coefficients $b_4 = b_5 = 0$ in (4.2b) and $c_4 = c_5 = c_6 = c_7 = 0$ in (4.2c). The resulting three equations in the system (4.3) is again reduced to two ODEs which further can be rewritten in the form of

$$\mathbf{K}\mathbf{t}' = \mathbf{t} \quad (4.11)$$

where $\mathbf{t} = [V, V', W, W', W'', W''']$ and $\mathbf{K} = \text{diag}(1, b_1, 1, 1, 1, c_{11})$. The IFOC boundary conditions for this case are

$$V(A^*) = W''(A^*) = W''''(A^*) = 0, \quad \text{and} \quad V(1) = W(1) = W'(1) = 0. \quad (4.12)$$

The ICOF boundary conditions are given by

$$V(A^*) = W(A^*) = W'(A^*) = 0, \quad \text{and} \quad V(1) = W''(1) = W''''(1) = 0. \quad (4.13)$$

5. Results

Before presenting the bifurcation solutions for hyperelastic annular plates, we compare the bifurcation results obtained by the current theory with the FvK plate theory in the small thickness regime for validation.

5.1. Growth-induced instability in a rectangular plate

Consider a rectangular plate of thickness $2H$ clamped at the ends $X = \pm 1$ (as shown in Fig. 5) subjected to a plane strain in the Y -direction and a Winkler foundation with effective stiffness K_0 at $Z = -2H$. Analytical results for this problem are derived by Wang et al. [54]. The Winkler foundation allows for analytical solution [81]. The plate is made up of an incompressible neo-Hookean material growing under uni-axial constant growth field for which the growth tensor takes the form $\mathbf{G} = \text{diag}(\lambda, 1, 1)$. The Winkler support provides traction only in the transverse direction at the bottom surface of the plate given as $t_3 = -K_0 \lambda W_0 = -K_0 \lambda [z^{(0)}/[2\bar{H}] + z^{(1)} + \bar{H} z^{(2)} + 2/3[\bar{H}]^2 z^{(3)} - 1]$ where \bar{H} is the ratio of plate thickness to length (in the X direction) i.e., $\bar{H} = H/L$, K_0 is the elastic constant of the foundation and W_0 is the transverse component of the displacement. We perturb the principal solution scaled by a small parameter ϵ ; $x^{(0)}(X) = X_0 + \epsilon U(X)$, $z^{(0)}(X) = -2\bar{H}(\lambda - 1) + \epsilon W(X)$ where $x^{(0)}$, $z^{(0)}$ are the deformed coordinates, and U and W are the displacements in axial and transverse direction, respectively. Upon substituting this ansatz in (2.11), equating (2.11b) to t_3 , and collecting only $O(\epsilon)$ terms, the governing plate differential equation is given by

$$\eta_1 W' + \eta_2 W'' + \eta_3 W^{iv} = 0, \quad (5.1)$$

subjected to clamped boundary conditions, $W'(\pm 1) = W''(\pm 1) = 0$. Here

$$\eta_1 = -\frac{\alpha \lambda}{2\bar{H}}, \\ \eta_2 = \frac{2}{\lambda} [1 - \lambda^4] - \bar{H} \alpha \lambda^3 + \frac{2\bar{H} \alpha \lambda^3}{1 + 3\lambda^4} [1 + \lambda^4],$$

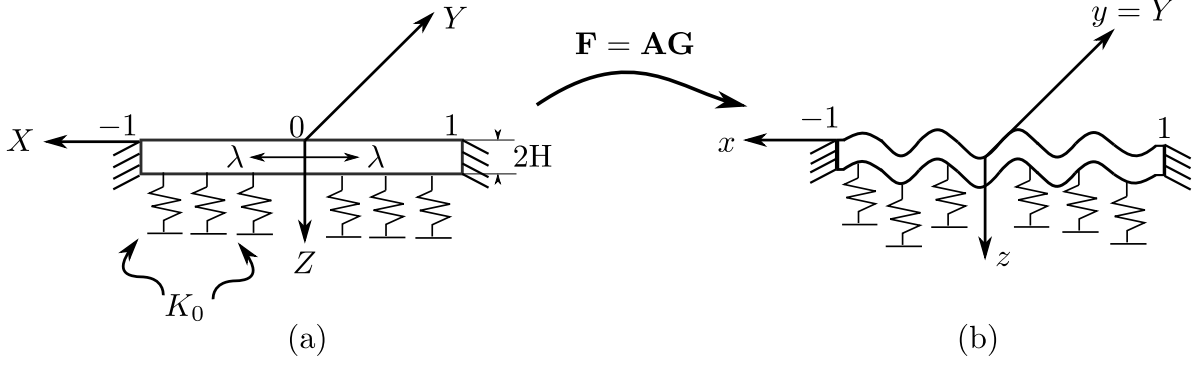


Fig. 5. Possible mode of buckling of a rectangular plate under growth-induced deformation. The plate is in a plane strain condition in the Y -direction and subjected to Winkler support with an effective stiffness, K_0 . The reference configuration (a) transforms to the deformed configuration (b) at the critical value of growth factor i.e., $\lambda = \lambda_{cr}$. Compression due to a constrained boundary leads to buckling of the plate.

Table 1

Comparison of bifurcation solution using finite-strain plate theory with analytical and numerical FvK plate results. The value of critical growth parameter λ_{cr} is compared for the plate thickness $\bar{h} = 0.015$ and associated mode numbers (n). The results are in good agreement with analytical results and close to the FvK results.

Mode number	$n = 7$	$n = 8$	$n = 5$	$n = 9$
FvK theory	1.01596	1.01712	1.01814	1.01916
Analytical results [54]	1.01626	1.01751	1.01839	1.01969
Current results	1.01626	1.01751	1.01839	1.01969

$$\eta_3 = -\frac{4\bar{H}^2(1+\lambda^4)}{(1+3\lambda^4)} \left[2\lambda^5 - 3\lambda^4 + 2\lambda - 1 \right] - \frac{4}{3}\bar{H}^2[1+\lambda^4] - \frac{4\bar{H}^3\alpha\lambda}{3[1+3\lambda^4]}[1+\lambda^4],$$

and $\alpha = K_0/C_0$ where $2C_0 = \mu$ is the ground state shear modulus of the hyperelastic material. We follow the same numerical scheme as described in Section 5.3 and obtained the bifurcation solution by numerically solving the GDE (5.1) for critical value of growth (λ_{cr}) responsible for the onset of instability. We compare our numerical results with the existing analytical results using current theory and numerical result using FvK plate theory provided by Wang et al. [54] in Table 1. The current numerical results are an almost exact match with the analytical solution and very close to the results obtained by the FvK theory.

5.2. Results for annular plate

The previous Section 4 discussed the possible type of perturbations (axisymmetry and asymmetric), corresponding ODEs and boundary conditions for the stability analysis. In this section, we numerically solve the derived ODEs to determine the critical growth factor at the onset of bifurcation. The numerical strategy used to derive the bifurcation solution is detailed in Section 5.3. We have shown only one set of bifurcation solutions in Section 5.3.1 when a plate is perturbed in R - Θ - Z direction and subjected to IFOC boundary condition. This is to illustrate the stability of buckling solution of the growing plate when perturbed. Then in Section 5.4, we compare the bifurcation solution of each type of perturbation considered in Section 4 and investigate the type of perturbation that results in the energetically preferred bifurcation solution. In the next Section 5.5, we have shown the comparison between the preferred bifurcation solutions for both boundary conditions.

5.3. Numerical bifurcation analysis of growing annular plate

In this section, we numerically solve the ODEs obtained in Section 4.1 for the critical growth factor (λ_{cr}) responsible for the onset of

instability. The numerical solutions of the resulting boundary value problems (BVPs) are computed using the compound matrix method [60,82] as well as the standard shooting method or determinant method [83,84]. Both the numerical methods are implemented in Matlab 2018a and the computed results are within a very small norm. However, the compound matrix method is much faster than the shooting method [85]. Equations are integrated using the ode45 ODE solver that implements an explicit Runge–Kutta method and then the fminsearchbnd optimisation subroutine [86] based on a Nelder–Mead simplex algorithm is used to minimise the errors.

5.3.1. Bifurcation solution for a plate with clamped outer edge condition

In this section, we evaluate the value of λ_{cr} for the first case as discussed in Section 4.1 i.e., perturbation along R - Θ - Z direction to demonstrate the behaviour of the bifurcation solution for an annular plate. For this, we numerically solve the system (4.3) subjected to IFOC boundary condition (4.4). The dependence of λ_{cr} on the plate thickness (\bar{h}) with different radius ratios $B/A = 1.1, 1.5, 2$ at various circumferential wavenumbers (m) is shown in Fig. 6. The λ_{cr} monotonically increases with \bar{h} suggesting that thicker plates with high bending stiffness require more growth to cause wrinkling instability. Furthermore, the magnitude of λ_{cr} decreases with the increase of B/A due to an apparent decrease in the boundary layer effects of the annular plate. We also observe that the critical wavenumber (m_{cr}) depends on the thickness, radius ratio, and boundary layer effects of the plate. Higher modes are energetically preferred for the low B/A values whereas lower modes are stable with an increasing value of B/A . For a plate with smaller radius ratio, $B/A = 1.1$, the obtained critical wavenumber is $m_{cr} = 22$ in the thin regime ($0.05 < \bar{h} < 0.1$), and $m_{cr} = 23$ in the thick regime ($\bar{h} > 0.1$). However, for $B/A = 1.5$ and 2 , the critical wavenumbers are $m_{cr} = 4$ and $m_{cr} = 2$, respectively.

5.4. Comparison between axisymmetric and asymmetric bifurcation

Here, we compare the bifurcation solutions for axisymmetric and asymmetric perturbations as discussed in Sections 4.1.1 and 4.1.2, respectively. The λ_{cr} is calculated by numerically solving the systems (4.7) and (4.11) subjected to the IFOC boundary conditions (4.8) and (4.12), respectively using the compound matrix method. Table 2 shows the dependence of λ_{cr} on plate thickness (\bar{h}) and plate radius ratio (B/A) at the corresponding critical mode number (m_{cr}) for each type of the considered perturbation. The bifurcation solution corresponding to axisymmetric (i.e., along R - Z) and asymmetric (i.e., along Θ - Z) perturbations to principal solution (3.4) follow a trend similar to the solution obtained in Section 5.3.1. The bifurcation solution corresponding to axisymmetric perturbation results in high λ_{cr} , thus requiring higher growth factor as compared to bifurcation solution associated with asymmetric perturbations.

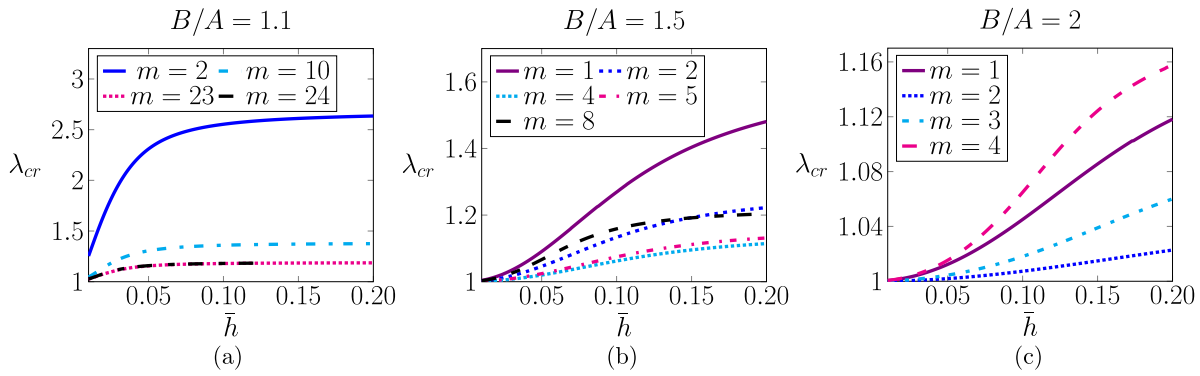


Fig. 6. Dependence of the critical growth factor on the thickness of the plate (\bar{h}) for various aspect ratios (a) $B/A = 1.1$, (b) $B/A = 1.5$, and (c) $B/A = 2$ that results in a perturbation in the radial-hoop-thickness direction. The bifurcation solution in each case is obtained for the IFOC boundary condition. Lowest value of λ_{cr} in each case corresponds to the minimum energy and therefore the preferable solution and determines the critical wave number m that directly relates to the number of wrinkles in the deformed configuration.

Table 2

Comparison of dependence of critical growth factor λ_{cr} on the dimensionless plate thickness (\bar{h}) at the corresponding critical circumferential wavenumber (m_{cr}) for plate radius ratio, $B/A = 1.1, 1.5, 2$. Critical value of the growth factor is obtained for both axisymmetric and asymmetric perturbations to the principal solution subjected to IFOC boundary constraint. The highlighted boxed values represent the lowest value of λ_{cr} and corresponds to the preferred bifurcation solution.

\bar{h}	$B/A = 1.1$			$B/A = 1.5$			$B/A = 2$		
	λ_{cr} (R-Z)	λ_{cr} (θ -Z)	λ_{cr} (R- θ -Z)	λ_{cr} (R-Z)	λ_{cr} (θ -Z)	λ_{cr} (R- θ -Z)	λ_{cr} (R-Z)	λ_{cr} (θ -Z)	λ_{cr} (R- θ -Z)
0.03	1.2106 ($m_{cr} = 16$)	1.1154 ($m_{cr} = 20$)	1.1127 ($m_{cr} = 20$)	1.0077 ($m_{cr} = 4$)	1.0074 ($m_{cr} = 4$)	1.0076 ($m_{cr} = 4$)	1.0007 ($m_{cr} = 2$)	1.0007 ($m_{cr} = 2$)	1.0007 ($m_{cr} = 2$)
0.05	1.4604 ($m_{cr} = 13$)	1.1619 ($m_{cr} = 22$)	1.1547 ($m_{cr} = 21$)	1.0214 ($m_{cr} = 4$)	1.0191 ($m_{cr} = 4$)	1.0200 ($m_{cr} = 4$)	1.0019 ($m_{cr} = 2$)	1.0019 ($m_{cr} = 2$)	1.0019 ($m_{cr} = 2$)
0.1	1.7893 ($m_{cr} = 10$)	1.1901 ($m_{cr} = 23$)	1.1793 ($m_{cr} = 22$)	1.0810 ($m_{cr} = 4$)	1.0551 ($m_{cr} = 4$)	1.0621 ($m_{cr} = 4$)	1.0075 ($m_{cr} = 2$)	1.0063 ($m_{cr} = 2$)	1.0073 ($m_{cr} = 2$)
0.15	1.8838 ($m_{cr} = 9$)	1.1959 ($m_{cr} = 24$)	1.1843 ($m_{cr} = 23$)	1.1477 ($m_{cr} = 4$)	1.0814 ($m_{cr} = 4$)	1.0955 ($m_{cr} = 4$)	1.0156 ($m_{cr} = 2$)	1.0113 ($m_{cr} = 2$)	1.0148 ($m_{cr} = 2$)
0.2	1.9162 ($m_{cr} = 9$)	1.1979 ($m_{cr} = 24$)	1.1860 ($m_{cr} = 23$)	1.1849 ($m_{cr} = 3$)	1.0962 ($m_{cr} = 4$)	1.1144 ($m_{cr} = 4$)	1.0247 ($m_{cr} = 2$)	1.0155 ($m_{cr} = 2$)	1.0228 ($m_{cr} = 2$)

For plates with $B/A = 1.5, 2$, the bifurcation solution obtained for the θ -Z perturbation has the minimum energy (highlighted values in Table 2 correspond to lowest values of λ_{cr} and therefore the preferred bifurcation solution) suggesting that the asymmetrically perturbed solution is energetically preferred. On the other hand, for a plate with low radius ratio $B/A = 1.1$, the bifurcation solution obtained for the R- θ -Z perturbation is energetically preferred. However, for small thickness values $\bar{h} \leq 0.05$, difference in the critical value λ_{cr} for each of the perturbation types is very small and it is hard to predict the preferred bifurcation mode. It is also observed that the critical wave number m_{cr} decreases with an increase in B/A for a fixed value of the plate thickness. This is expected since thinner rings (low B/A) have a larger circumference in relation to their surface area and therefore tend to develop more wrinkles compared to bulkier rings (high B/A) and is corroborated by the experimental and analytical findings of Mora and Boudaoud [50] and Liu et al. [79].

For $B/A = 1.1$, the critical load λ_{cr} and the corresponding m_{cr} increase with the thickness \bar{h} . For higher B/A values, m_{cr} remains constant but only λ_{cr} increases with the thickness \bar{h} . In general higher thickness value \bar{h} results in larger compressive stresses at the bifurcation point due to a larger value of λ_{cr} which is discussed in the subsequent section. As a result, bifurcation occurs with a higher wavenumber m_{cr} for $B/A = 1.1$ as \bar{h} increases. For $B/A = 1.5, 2$, the change in λ_{cr} with the \bar{h} value is not significant and as a result m_{cr} stays constant.

We conclude that the θ -Z (asymmetric) type of perturbation is appropriate for the annular plate with moderate and high radius ratio when subjected to IFOC condition as compared to other perturbations. In the subsequent section, we analyse the influence of IFOC boundary

condition (i.e., inner edge of the plate is clamped) on the bifurcation solutions obtained using all types of considered perturbations and compare these results with the IFOC results.

5.5. Influence of boundary condition on the buckling solution

In this section, we evaluate λ_{cr} for an annular plate considering all type of perturbations by numerically solving (4.3), (4.7), and (4.11) subjected to IFOC conditions (4.5), (4.9), and (4.13), respectively and compare with the solutions obtained in the previous section. The values of λ_{cr} are compared for each type of perturbation and then we identify the preferred bifurcation solution by studying the lowest value of λ_{cr} (at the corresponding m_{cr}). Table 3 shows the dependence of preferred bifurcation solution (lowest λ_{cr}) on plate thickness (\bar{h}) and radius ratio B/A when the growing plate is subjected to IFOC boundary condition. This table also compares the lowest values of λ_{cr} of the plate subjected to IFOC condition (highlighted in Table 2) with the obtained IFOC results. We observe that the variation of λ_{cr} with plate thickness (\bar{h}) and radius ratio (B/A) for both the boundary conditions is quite similar. We also observe that for the plates subjected to IFOC boundary condition, the bifurcation solution associated with R- θ -Z perturbation have minimum energy and is preferable over other type of perturbations.

Unlike the IFOC case, the values of m_{cr} and λ_{cr} increase with \bar{h} for all values of B/A . This can be visualised by plotting the variation of λ_{cr} with m for various values of \bar{h} in Figs. 7a and 7b. The critical wavenumber (corresponding to the minima of these curves) is constant with \bar{h} for the annular plate ($B/A = 1.5, 2$) subjected to IFOC boundary condition as discussed in previous section. However, the m_{cr} increases with the \bar{h} for fixed B/A using IFOC boundary condition. This suggest

Table 3

Dependence of the critical value of growth factor (λ_{cr}) on plate thickness (\bar{h}), radius ratio (B/A), and critical wavenumber (m_{cr}). The lowest value of λ_{cr} is obtained for the annular plate with aspect ratio $B/A = 1.1, 1.5, 2$ at various plate thickness \bar{h} subjected to IFOC and ICOF boundary conditions. The preferred bifurcation solution for ICOF boundary condition is obtained using R - θ - Z perturbation. For IFOC boundary condition, R - θ - Z and θ - Z perturbation are preferred for $B/A = 1.1$ and $B/A = 1.5, 2$, respectively.

\bar{h}	$B/A = 1.1$		$B/A = 1.5$		$B/A = 2$	
	λ_{cr} (IFOC)	λ_{cr} (ICOF)	λ_{cr} (IFOC)	λ_{cr} (ICOF)	λ_{cr} (IFOC)	λ_{cr} (ICOF)
0.03	1.1127 ($m_{cr} = 20$) (R - θ - Z)	1.1327 ($m_{cr} = 23$) (R - θ - Z)	1.0074 ($m_{cr} = 4$) (θ - Z)	1.0386 ($m_{cr} = 6$) (R - θ - Z)	1.0007 ($m_{cr} = 2$) (θ - Z)	1.0306 ($m_{cr} = 4$) (R - θ - Z)
0.05	1.1547 ($m_{cr} = 21$) (R - θ - Z)	1.1680 ($m_{cr} = 26$) (R - θ - Z)	1.0191 ($m_{cr} = 4$) (θ - Z)	1.0816 ($m_{cr} = 6$) (R - θ - Z)	1.0019 ($m_{cr} = 2$) (θ - Z)	1.0681 ($m_{cr} = 4$) (R - θ - Z)
0.1	1.1793 ($m_{cr} = 22$) (R - θ - Z)	1.1850 ($m_{cr} = 30$) (R - θ - Z)	1.0551 ($m_{cr} = 4$) (θ - Z)	1.1493 ($m_{cr} = 7$) (R - θ - Z)	1.0063 ($m_{cr} = 2$) (θ - Z)	1.1387 ($m_{cr} = 5$) (R - θ - Z)
0.15	1.1843 ($m_{cr} = 23$) (R - θ - Z)	1.1879 ($m_{cr} = 32$) (R - θ - Z)	1.0814 ($m_{cr} = 4$) (θ - Z)	1.1690 ($m_{cr} = 9$) (R - θ - Z)	1.0113 ($m_{cr} = 2$) (θ - Z)	1.1624 ($m_{cr} = 6$) (R - θ - Z)
0.2	1.1860 ($m_{cr} = 23$) (R - θ - Z)	1.1888 ($m_{cr} = 48$) (R - θ - Z)	1.0962 ($m_{cr} = 4$) (θ - Z)	1.1727 ($m_{cr} = 14$) (R - θ - Z)	1.0155 ($m_{cr} = 2$) (θ - Z)	1.1705 ($m_{cr} = 6$) (R - θ - Z)

that a preferred bifurcation solution (satisfying the ICOF boundary conditions with R - θ - Z perturbation) consist of more wrinkles in hoop direction for thicker plates at high value of λ_{cr} . The contour plots with normalised displacement demonstrate the number of wrinkles in the circumferential direction at the bifurcation point. For the plate with $B/A = 1.5$ and $\bar{h} = 0.2$ subjected to IFOC boundary condition, the critical wavenumber (m_{cr}) is 4 and does not change with the thickness. Whereas, for the plate of $B/A = 1.5$, $\bar{h} = 0.05$ subjected to ICOF boundary condition, the m_{cr} is 6 and for the plate with $\bar{h} = 0.2$, the m_{cr} is 14 which shows the increase in number of wrinkles with \bar{h} . This is due to the expansion of the unconstrained outer boundary $b > B$ (considering ICOF) with the increase of thickness under growth stretch ($\lambda > 1$). The deformed configuration results in a larger circumference which can accommodate more number of wrinkles in the buckled configuration.

Fig. 7c shows the variation of transverse amplitude of the mode shape along the radius of the plate for different thickness at same radius ratio $B/A = 1.5$. In the case of IFOC, the mode shape variation remains the same for all plate thickness considered. In the case of ICOF, for thin plates ($m_{cr} = 6$), the radial extent of wrinkles is considerable i.e., the amplitude variation along the radius is more, whereas for thick plates the amplitude variation is localised at the unconstrained outer edge (as shown in Fig. 7b). Thus, in the case of ICOF, the boundary layer effects are observed to be significant for thick plates when compared to thin plates.

Next, we investigate the effect of compressive stress on the wrinkle formation along the boundaries of annular plate. Figs. 7d and 7e shows the variation of normalised maximum stress (\tilde{P}_{max}/C_0) with the plate radius ratio at different plate thickness values ($\bar{h} = 0.03, 0.1$) for IFOC and ICOF boundary conditions, respectively. The blue and red curves represents the dimensionless radial stress ($\tilde{P}_{rad}/C_0 = \tilde{P}_{RR}$) and circumferential stress ($\tilde{P}_{hoop}/C_0 = \tilde{P}_{\theta\theta}$), respectively. The variation of maximum stress with aspect ratio shows the similar behaviour for IFOC and ICOF case however, we observe that for IFOC condition, both the \tilde{P}_{RR} and $\tilde{P}_{\theta\theta}$ are compressive which promotes the bifurcation where as for ICOF boundary condition, $\tilde{P}_{\theta\theta}$ is compressive and \tilde{P}_{RR} is tensile that delays the bifurcation (Mathematical expressions for stresses are detailed in the supplementary document). Here, we plot the maximum stress value to show the dependence of stresses on the geometry of plate. Considering ICOF condition, for a fixed value of B/A , the value of critical growth stretch increases with the increase

of thickness (due to increased bending stiffness), as shown in Table 3 which yields high compressive stresses as shown in Figs. 7d and 7e which results in more number of wrinkles. Whereas, the converse behaviour of stress is observed with respect to increase in the radius ratio of the annular plate for a fixed value of plate thickness that is the critical stretch value and compressive stresses decrease with the increase in radius ratio suggesting less wrinkles. For plates with low B/A value, both the compressive stress and boundary layer effects govern the wrinkle formation. For plates with high B/A value, only the compressive stress governs the wrinkle formation. Thus, the combined effect of compressive stresses and boundary layer effects govern the number of wrinkles and their localisation along the boundaries of the thick plate. Also, the results show that the magnitude of λ_{cr} and m_{cr} is higher for the bifurcation solution associated with ICOF case when compared to IFOC. For the same geometric parameters $B/A = 1.5$ and $\bar{h} = 0.1$, the value of λ_{cr} associated with IFOC condition is 1.0551 at $m_{cr} = 4$ and ICOF condition is $\lambda_{cr} = 1.1493$ at $m_{cr} = 7$.

5.5.1. Comparison with computational results for growing annulus

We have discussed in Section 3.2 that current plate theory estimates pre-buckling results for circular ring and annular shell. Now, to test the accuracy of numerical framework, we compare the bifurcation solution of the annular plate using current theory with the computational results for a nearly incompressible (Poisson ratio = 0.495) neo-Hookean growing annulus provided by Groh [65] using the finite element method. He used a seven-parameter quadrilateral shell element to analyse the growth-induced instability in thin growing shell by implementing the numerical continuation algorithm. In his work, the isotropic planar growth tensor is given as $\mathbf{G} = \text{diag}(1 + \lambda_g, 1 + \lambda_g, 1)$. The prescribed boundary condition were pinned inner edge and free outer edge. He reported the critical value of growth function and wavenumber for growing annulus as $\lambda_{gcr} = 0.137 \times 10^{-5}$ and $m_{cr} = 3$, respectively. For the same parameters, radius ratio ($B/A = 2$), shell thickness ($2h = 0.001 \rightarrow 2\bar{h} = 0.0005$), and the boundary conditions which are $U(A^*) = V(A^*) = W(A^*) = W''(A^*) = 0$ (corresponding to simply supported inner boundary) and $U'(1) = V'(1) = W'(1) = W'''(1) = 0$ (corresponding to free outer boundary), the current incompressible plate theory yields the critical wavenumber $m_{cr} = 3$ with $\lambda_{gcr} = 0.152 \times 10^{-5}$. The two results are relatively close to each other with a small deviation arising due to the non satisfaction of incompressibility constraint in Groh [65]'s formulation.

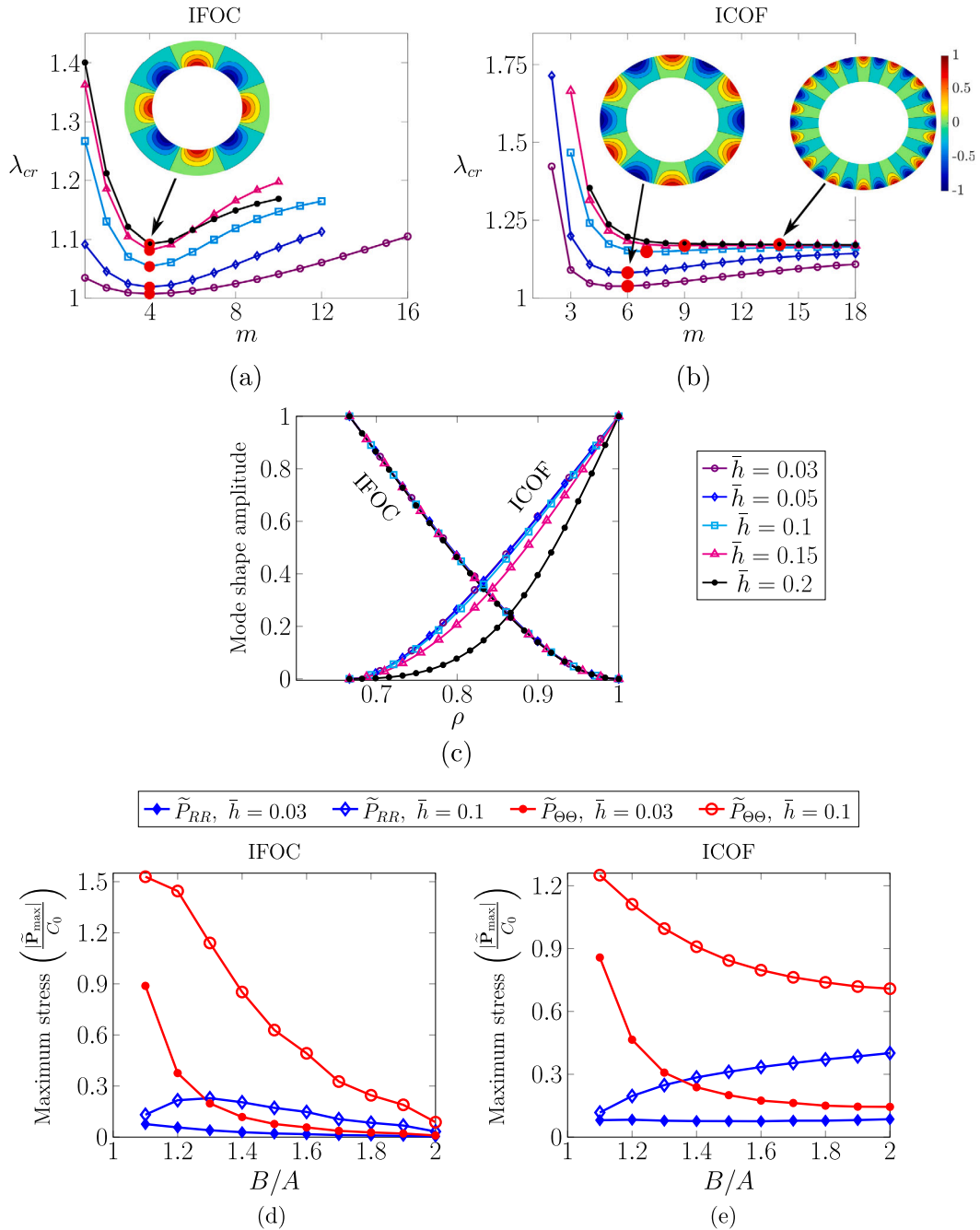


Fig. 7. (a) and (b) Dependence of the critical growth factor λ_{cr} on the wavenumber m for an annular plate with aspect ratio $B/A = 1.5$ subjected to IFOC (θ - Z perturbation) and ICOF (R - θ - Z perturbation) boundary conditions, respectively. For each plate thickness value \bar{h} , the red marks highlight the critical value of wavenumber (m_{cr}) corresponding to the lowest value of λ_{cr} on the solution curve. Normalised 2-D displacement contours at bifurcation for the IFOC boundary condition is plotted at $\bar{h} = 0.2$, $m_{cr} = 4$, $\lambda_{cr} = 1.0962$. Similar contours for the ICOF boundary condition are plotted at $m_{cr} = 6$, $\lambda_{cr} = 1.0816$ and $m_{cr} = 14$, $\lambda_{cr} = 1.1727$ for $\bar{h} = 0.05$ and $\bar{h} = 0.2$, respectively. (c) Variation of the transverse amplitude of the mode shapes with the radius of the plate corresponding to the highlighted marks in (a) and (b). For thick plate subjected to ICOF condition ($\bar{h} = 0.2$, $m_{cr} = 14$), the radial extent of wrinkles is small suggesting that the wrinkles are more localised towards the outer unconstrained boundary of the plate. (d) and (e) Variation of normalised maximum stress components ($|\tilde{P}_{max}|/C_0$) with plate aspect ratio and thickness for IFOC and ICOF case, respectively. The blue and red curve represents the radial (\tilde{P}_{RR}) and hoop ($\tilde{P}_{\theta\theta}$) stress distribution. The filled and unfilled markers represents the maximum stress at $\bar{h} = 0.03$ and $\bar{h} = 0.1$, respectively.

6. Conclusion

In this work, we have investigated the wrinkling phenomena in growing hyperelastic annular plates using a finite-strain asymptotic plate theory. A 3-D plate equilibrium system is reduced to 2-D plate governing system by adopting series expansion along the thickness direction. A homogeneous isotropic growth function is considered as a control parameter in inducing the circumferential instability in an incompressible neo-Hookean annular plate. To validate the 2-D plate

framework, we compared the numerical pre-buckling solution for a very thin annular plate with the analytical pre-buckling solution of circular ring. Both the analytical and numerical results are in good agreement. We carried out linear bifurcation analysis with asymmetric (i.e., along R - θ - Z and θ - Z direction) as well as axisymmetric perturbations (i.e., along R - Z direction) for two cases of boundary conditions (IFOC and ICOF). The numerical solution of resulting system of ODEs in each case is solved using the compound matrix method. The critical value of growth factor (λ_{cr}) and the associated wavenumber (m_{cr})

is evaluated for each type of perturbation and boundary conditions. We observe that the bifurcation solution corresponding to asymmetric perturbation is preferred for both boundary conditions as it has a lower value of λ_{cr} when compared to the axisymmetric perturbation. The bifurcation solutions associated with IFOC and ICOF boundary conditions exhibit a similar behaviour for variation of λ_{cr} (at m_{cr}) with B/A and \bar{h} . However, the magnitude of λ_{cr} is lower for the case of IFOC when compared to ICOF due to the presence of compressive radial and circumferential stresses which promotes wrinkling. In addition, for ICOF case, we find that for a fixed value of B/A , the deformed radius and λ_{cr} increases with plate thickness resulting in higher compressive stress in circumferential direction which further results in more number of localised wrinkles along the outer circumference of the thicker plate. To test the accuracy of obtained results for annular plate, we compare the bifurcation solution obtained for incompressible annular plate with the existing bifurcation solution for slightly incompressible shell obtained using finite element approach. Both the bifurcation results are close to each other showing the consistency of current plate theory.

Furthermore, we have restricted our study to determine the critical value of growth factor responsible for the onset of wrinkling, however a post-bifurcation analysis may provide insights on the evolution of wrinkle deformation with growth. This is currently being investigated and our findings will be reported in a suitable forum at a later stage.

CRedit authorship contribution statement

Sumit Mehta: Methodology, Software, Validation, Formal analysis, Investigation, Writing – original draft, Visualization. **Gangadharan Raju:** Conceptualization, Methodology, Validation, Formal analysis, Writing – review & editing, Project administration. **Prashant Saxena:** Conceptualization, Methodology, Validation, Formal analysis, Writing – review & editing, Project administration, Funding acquisition.

Declaration of competing interest

The authors declare that they have no known competing financial interests or personal relationships that could have appeared to influence the work reported in this paper.

Acknowledgements

Prashant Saxena acknowledges the financial support of the EPSRC, UK grant no. EP/V030833/1.

Appendix A. Expression for Piola stress and unknown variables

The series expansion of deformation gradient (**F**), elastic deformation (**A**), inverse transpose of Growth tensor (**G**^{-T}) and Piola Kirchhoff (**P**) tensor are given by

$$\mathbf{F} = \sum_{n=0}^2 \frac{Z^n}{n!} \mathbf{F}^{(n)}(\zeta) + O(Z^3), \quad \mathbf{A} = \sum_{n=0}^2 \frac{Z^n}{n!} \mathbf{A}^{(n)}(\zeta) + O(Z^3),$$

$$\mathbf{G}^{-T} = \sum_{n=0}^2 \frac{Z^n}{n!} \tilde{\mathbf{G}}^n(\zeta) + O(Z^3), \quad \mathbf{P} = \sum_{n=0}^2 \frac{Z^n}{n!} \mathbf{P}^{(n)}(\zeta) + O(Z^3).$$
(A.1)

For an incompressible neo-Hookean material elastic strain energy function is $\phi_0(\mathbf{A}) = C_0[\text{tr}(\mathbf{A}^T \mathbf{A}) - 3]$ and the associated Piola Kirchhoff stress is given as, $\mathbf{P} = J_G [2C_0[\mathbf{A}] - p\mathbf{A}^{-T}] \mathbf{G}^{-T}$. Then, the first term in right side of the expression for **P** in (A.1) is obtained as

$$\mathbf{P}^{(0)} = J_G [2C_0\mathbf{A}^{(0)} - p\mathbf{A}^{(0)-T}] \tilde{\mathbf{G}}^{(0)}. \tag{A.2}$$

By using bottom traction condition, $\mathbf{P}^{(0)}\mathbf{k} = \mathbf{0}$ and substituting the expression for **A**⁽⁰⁾ (see (2.6)) in (A.2) we obtain

$$2C_0 \nabla \mathbf{x}^{(0)} \tilde{\mathbf{G}}^{(0)T} \tilde{\mathbf{G}}^{(0)} \mathbf{k} + 2C_0 J_G \left| \tilde{\mathbf{G}}^{(0)} \mathbf{k} \right|^2 \mathbf{x}^{(1)} - p^{(0)} \mathbf{F}^{(0)*} \mathbf{k} = \mathbf{0}, \tag{A.3}$$

where $J^{(0)} = J_G|_{Z=0}$, $\tilde{\mathbf{G}}^{(0)} = J^{(0)}\tilde{\mathbf{G}}^{(0)}$, and $\mathbf{F}^{(0)*} = \text{Cofac}(\mathbf{F}^{(0)})$. In this work, we use $\nabla \mathbf{x}^{(0)*}$ in place of $\mathbf{F}^{(0)*}\mathbf{k}$ which is given as

$$\begin{aligned} \nabla \mathbf{x}^{(0)*} = & \frac{r^{(0)}}{R} \left[\frac{\partial \theta^{(0)}}{\partial R} \frac{\partial z^{(0)}}{\partial \theta} - \frac{\partial \theta^{(0)}}{\partial \theta} \frac{\partial z^{(0)}}{\partial R} \right] \mathbf{e}_1 \\ & + \frac{1}{R} \left[\frac{\partial r^{(0)}}{\partial \theta} \frac{\partial z^{(0)}}{\partial R} - \frac{\partial r^{(0)}}{\partial R} \frac{\partial z^{(0)}}{\partial \theta} \right] \mathbf{e}_2 \\ & + \frac{r^{(0)}}{R} \left[\frac{\partial r^{(0)}}{\partial R} \frac{\partial \theta^{(0)}}{\partial \theta} - \frac{\partial \theta^{(0)}}{\partial R} \frac{\partial r^{(0)}}{\partial \theta} \right] \mathbf{k}. \end{aligned} \tag{A.4}$$

Using incompressibility constraint $\det(\mathbf{A}) = 1$, we obtain $\det(\mathbf{F}^{(0)}) = \det(\tilde{\mathbf{G}}^{(0)-T})$ which result in

$$\mathbf{x}^{(1)} \cdot \nabla \mathbf{x}^{(0)*} = \det \left(\tilde{\mathbf{G}}^{(0)-T} \right), \tag{A.5}$$

where $\det(\mathbf{F}^{(0)}) = \left[r^{(1)}\mathbf{e}_1 + r^{(0)}\theta^{(1)}\mathbf{e}_2 + z^{(1)}\mathbf{e}_3 \right] \cdot \mathbf{F}^{(0)*}\mathbf{k} = \mathbf{x}^{(1)} \cdot \nabla \mathbf{x}^{(0)*}$. Using (A.3) we obtain the explicit expression for $\mathbf{x}^{(1)}$

$$\mathbf{x}^{(1)} = \frac{-2C_0 \nabla \mathbf{x}^{(0)} \tilde{\mathbf{G}}^{(0)T} \tilde{\mathbf{G}}^{(0)} \mathbf{k} + p^{(0)} \nabla \mathbf{x}^{(0)*}}{2C_0 J_G \left| \tilde{\mathbf{G}}^{(0)} \mathbf{k} \right|^2}. \tag{A.6}$$

To obtain the explicit expression for $p^{(0)}$ we substitute (A.6) into (A.5) which yields

$$p^{(0)} = \frac{2C_0 J_G \left| \tilde{\mathbf{G}}^{(0)} \mathbf{k} \right|^2}{\det \tilde{\mathbf{G}}^{(0)T} \left| \nabla \mathbf{x}^{(0)*} \right|^2} + \left[2C_0 \nabla \mathbf{x}^{(0)} \tilde{\mathbf{G}}^{(0)T} \tilde{\mathbf{G}}^{(0)} \mathbf{k} \right] \cdot \frac{\nabla \mathbf{x}^{(0)*}}{\left| \nabla \mathbf{x}^{(0)*} \right|^2}. \tag{A.7}$$

Using Eq. (A.7), we obtain the expression for $p^{(0)}$ which is

$$p^{(0)} = \frac{2C_0 \lambda^4}{\left| \nabla \mathbf{x}^{(0)*} \right|^2}, \tag{A.8}$$

where $\nabla \mathbf{x}^{(0)*} = \Delta x_{11}\mathbf{e}_1 + \Delta x_{22}\mathbf{e}_2 + \Delta x_{33}\mathbf{k}$ is given by (A.4). On substituting $p^{(0)}$ in (A.6) we obtain explicit expressions for $r^{(1)}$, $\theta^{(1)}$, and $z^{(1)}$ as

$$r^{(1)} = \frac{p^{(0)} \Delta x_{11}}{2C_0 \lambda^2}, \quad \theta^{(1)} = \frac{p^{(0)} \Delta x_{22}}{2C_0 \lambda^2 r^{(0)}}, \quad \text{and} \quad z^{(1)} = \frac{p^{(0)} \Delta x_{33}}{2C_0 \lambda^2}. \tag{A.9}$$

Appendix B. Supplementary data

Supplementary material related to this article can be found online at <https://doi.org/10.1016/j.ijmeccsci.2022.107481>.

References

- [1] Li B, Cao Y-P, Feng X-Q, Gao H. Mechanics of morphological instabilities and surface wrinkling in soft materials: a review. *Soft Matter* 2012;8(21):5728–45.
- [2] Dai H-H, Liu Y. Critical thickness ratio for buckled and wrinkled fruits and vegetables. *Europhys Lett* 2014;108(4):44003.
- [3] Coen E, Rolland-Lagan A-G, Matthews M, Bangham JA, Prusinkiewicz P. The genetics of geometry. *Proc Natl Acad Sci* 2004;101(14):4728–35.
- [4] Ambrosi D, Ateshian GA, Arruda EM, Cowin S, Dumais J, Goriely A, et al. Perspectives on biological growth and remodeling. *J Mech Phys Solids* 2011;59(4):863–83.
- [5] Wiggs BR, Hrousis CA, Drazen JM, Kamm RD. On the mechanism of mucosal folding in normal and asthmatic airways. *J Appl Physiol* 1997;83(6):1814–21.
- [6] Raybaud C, Widjaja E. Development and dysgenesis of the cerebral cortex: malformations of cortical development. *Neuroimag. Clin.* 2011;21(3):483–543.
- [7] Cerda E. Mechanics of scars. *J Biomech* 2005;38(8):1598–603.
- [8] Nassar D, Letavernier E, Baud L, Aractingi S, Khosrotehrani K. Calpain activity is essential in skin wound healing and contributes to scar formation. *PLoS One* 2012;7(5):e37084.
- [9] Ben Amar M, Goriely A. Growth and instability in elastic tissues. *J Mech Phys Solids* 2005;53(10):2284–319.
- [10] Liang H, Mahadevan L. Growth, geometry, and mechanics of a blooming lily. *Proc Natl Acad Sci* 2011;108(14):5516–21.
- [11] Cao Y, Jiang Y, Li B, Feng X. Biomechanical modeling of surface wrinkling of soft tissues with growth-dependent mechanical properties. *Acta Mech Solida Sin* 2012;25(5):483–92.
- [12] Budday S, Steinmann P, Kuhl E. The role of mechanics during brain development. *J Mech Phys Solids* 2014;72:75–92.
- [13] Balbi V, Ciarletta P. Morpho-elasticity of intestinal villi. *J R Soc Interface* 2013;10(82):20130109.

- [14] Limbert G, Kuhl E. On skin microrelief and the emergence of expression micro-wrinkles. *Soft Matter* 2018;14(8):1292–300.
- [15] Ionov L. Biomimetic hydrogel-based actuating systems. *Adv Funct Mater* 2013;23(36):4555–70.
- [16] Cao Y, Hutchinson JW. From wrinkles to creases in elastomers: the instability and imperfection-sensitivity of wrinkling. *Proc R Soc A* 2012;468(2137):94–115.
- [17] Kempaiah R, Nie Z. From nature to synthetic systems: shape transformation in soft materials. *J Mater. Chem. B* 2014;2(17):2357–68.
- [18] Khang D-Y, Rogers JA, Lee HH. Mechanical buckling: mechanics, metrology, and stretchable electronics. *Adv Funct Mater* 2009;19(10):1526–36.
- [19] Terwagne D, Brojan M, Reis PM. Smart morphable surfaces for aerodynamic drag control. *Adv Mater* 2014;26(38):6608–11.
- [20] Rogers JA, Someya T, Huang Y. Materials and mechanics for stretchable electronics. *Science* 2010;327(5973):1603–7.
- [21] Stein-Montalvo L, Costa P, Pezulla M, Holmes DP. Buckling of geometrically confined shells. *Soft Matter* 2019;15(6):1215–22.
- [22] Kuhl E. Growing matter: a review of growth in living systems. *J Mech Behav Biomed Mater* 2014;29:529–43.
- [23] Goriely A. The mathematics and mechanics of biological growth, vol. 45. Springer; 2017.
- [24] Rodriguez EK, Hoger A, McCulloch AD. Stress-dependent finite growth in soft elastic tissues. *J Biomech* 1994;27(4):455–67.
- [25] Du Y, Lü C, Chen W, Destrade M. Modified multiplicative decomposition model for tissue growth: beyond the initial stress-free state. *J Mech Phys Solids* 2018;118:133–51.
- [26] Du Y, Lü C, Destrade M, Chen W. Influence of initial residual stress on growth and pattern creation for a layered aorta. *Sci Rep* 2019;9(1):1–9.
- [27] Garikipati K, Arruda EM, Grosh K, Narayanan H, Calve S. A continuum treatment of growth in biological tissue: the coupling of mass transport and mechanics. *J Mech Phys Solids* 2004;52(7):1595–625.
- [28] Goriely A, Ben Amar M. On the definition and modeling of incremental, cumulative, and continuous growth laws in morphoelasticity. *Biomech Model Mechanobiol* 2007;6(5):289–96.
- [29] Goriely A, Ben Amar M. Differential growth and instability in elastic shells. *Phys Rev Lett* 2005;94(19):198103.
- [30] Moulton D, Goriely A. Circumferential buckling instability of a growing cylindrical tube. *J Mech Phys Solids* 2011;59(3):525–37.
- [31] Wu M, Ben Amar M. Growth and remodelling for profound circular wounds in skin. *Biomech Model Mechanobiol* 2015;14(2):357–70.
- [32] Liu Y, Zhang Z, Devillanova G, Cai Z. Surface instabilities in graded tubular tissues induced by volumetric growth. *Int J Non-Linear Mech* 2020;127:103612.
- [33] Liu R-C, Liu Y, Cai Z. Influence of the growth gradient on surface wrinkling and pattern transition in growing tubular tissues. *Proc R Soc Lond Ser A* 2021;477(2254):20210441.
- [34] Li B, Xu G-K, Feng X-Q. Tissue-growth model for the swelling analysis of core-shell hydrogels. *Soft Mater.* 2013;11(2):117–24.
- [35] Papastavrou A, Steinmann P, Kuhl E. On the mechanics of continua with boundary energies and growing surfaces. *J Mech Phys Solids* 2013;61(6):1446–63.
- [36] Swain D, Gupta A. Interfacial growth during closure of a cutaneous wound: stress generation and wrinkle formation. *Soft Matter* 2015;11(32):6499–508.
- [37] Swain D, Gupta A. Mechanics of cutaneous wound rupture. *J Biomech* 2016;49(15):3722–30.
- [38] Jia F, Pearce SP, Goriely A. Curvature delays growth-induced wrinkling. *Phys Rev E* 2018;98(3):033003.
- [39] Wang T, Yang Y, Fu C, Liu F, Wang K, Xu F. Wrinkling and smoothing of a soft shell. *J Mech Phys Solids* 2020;134:103738.
- [40] Coman CD, Haughton D. Localized wrinkling instabilities in radially stretched annular thin films. *Acta Mech* 2006;185(3):179–200.
- [41] Coman CD, Matthews MT, Bassom AP. Asymptotic phenomena in pressurized thin films. *Proc R Soc A* 2015;471(2182):20150471.
- [42] Li B, Huang S-Q, Feng X-Q. Buckling and postbuckling of a compressed thin film bonded on a soft elastic layer: a three-dimensional analysis. *Arch Appl Mech* 2010;80(2):175–88.
- [43] Mihai LA, Goriely A. A plate theory for nematic liquid crystalline solids. *J Mech Phys Solids* 2020;144:104101.
- [44] Dervaux J, Ciarletta P, Ben Amar M. Morphogenesis of thin hyperelastic plates: a constitutive theory of biological growth in the Föppl-von Kármán limit. *J Mech Phys Solids* 2009;57(3):458–71.
- [45] Efrati E, Sharon E, Kupferman R. Elastic theory of unconstrained non-Euclidean plates. *J Mech Phys Solids* 2009;57(4):762–75.
- [46] Pezulla M, Smith GP, Nardinocchi P, Holmes DP. Geometry and mechanics of thin growing bilayers. *Soft Matter* 2016;12(19):4435–42.
- [47] Dias MA, Hanna JA, Santangelo CD. Programmed buckling by controlled lateral swelling in a thin elastic sheet. *Phys Rev E* 2011;84(3):036603.
- [48] Jones GW, Mahadevan L. Optimal control of plates using incompatible strains. *Nonlinearity* 2015;28(9):3153.
- [49] Holmes DP. Elasticity and stability of shape-shifting structures. *Curr. Opin. Colloid Interface Sci.* 2019;40:118–37.
- [50] Mora T, Boudaoud A. Buckling of swelling gels. *Euro. Phys. J. E* 2006;20(2):119–24.
- [51] Kienzler R. On consistent plate theories. *Arch Appl Mech* 2002;72(4):229–47.
- [52] Dai H-H, Song Z. On a consistent finite-strain plate theory based on three-dimensional energy principle. *Proc R Soc A* 2014;470(2171):20140494.
- [53] Wang J, Song Z, Dai H-H. On a consistent finite-strain plate theory for incompressible hyperelastic materials. *Int J Solids Struct* 2016;78:101–9.
- [54] Wang J, Steigmann D, Wang F-F, Dai H-H. On a consistent finite-strain plate theory of growth. *J Mech Phys Solids* 2018;111:184–214.
- [55] Wang J, Wang Q, Dai H-H, Du P, Chen D. Shape-programming of hyperelastic plates through differential growth: an analytical approach. *Soft Matter* 2019;15(11):2391–9.
- [56] Du P, Dai H-H, Wang J, Wang Q. Analytical study on growth-induced bending deformations of multi-layered hyperelastic plates. *Int J Non-Linear Mech* 2020;119:103370.
- [57] Wang J, Li Z, Jin Z. A theoretical scheme for shape-programming of thin hyperelastic plates through differential growth. *Math Mech Solids* 2022;10812865221089694.
- [58] Chen X, Dai H-H. Stress-free configurations induced by a family of locally incompatible growth functions. *J Mech Phys Solids* 2020;137:103834.
- [59] Liu Y, Ma W, Dai H-H. On a consistent finite-strain plate model of nematic liquid crystal elastomers. *J Mech Phys Solids* 2020;145:104169.
- [60] Mehta S, Raju G, Saxena P. Growth induced instabilities in a circular hyperelastic plate. *Int J Solids Struct* 2021;226:111026.
- [61] Vandiver R, Goriely A. Differential growth and residual stress in cylindrical elastic structures. *Phil Trans R Soc A* 2009;367(1902):3607–30.
- [62] Saez P. On the theories and numerics of continuum models for adaptation processes in biological tissues. *Arch Comput Methods Eng* 2016;23(2):301–22.
- [63] Dortdivanlioglu B, Javili A, Linder C. Computational aspects of morphological instabilities using isogeometric analysis. *Comput Methods Appl Mech Eng* 2017;316:261–79.
- [64] Zheng Y, Wang J, Ye H, Liu Y, Zhang H. A solid-shell based finite element model for thin-walled soft structures with a growing mass. *Int J Solids Struct* 2019;163:87–101.
- [65] Groh RM. A morphoelastic stability framework for post-critical pattern formation in growing thin biomaterials. *Comput Methods Appl Mech Eng* 2022;394:114839.
- [66] Kadapa C, Li Z, Hossain M, Wang J. On the advantages of mixed formulation and higher-order elements for computational morphoelasticity. *J Mech Phys Solids* 2021;148:104289.
- [67] Liang H, Mahadevan L. The shape of a long leaf. *Proc Natl Acad Sci* 2009;106(52):22049–54.
- [68] Steele CR. Shell stability related to pattern formation in plants. *J Appl Mech* 2000;67(2):237–47.
- [69] Flynn C, McCormack BA. A simplified model of scar contraction. *J Biomech* 2008;41(7):1582–9.
- [70] Tallinen T, Biggins JS. Mechanics of invagination and folding: Hybridized instabilities when one soft tissue grows on another. *Phys Rev E* 2015;92(2):022720.
- [71] Jin L, Cai S, Suo Z. Creases in soft tissues generated by growth. *Europhys Lett* 2011;95(6):64002.
- [72] Wang Q, Zhao X. A three-dimensional phase diagram of growth-induced surface instabilities. *Sci Rep* 2015;5(1):1–10.
- [73] Yang P, Fang Y, Yuan Y, Meng S, Nan Z, Xu H, et al. A perturbation force based approach to creasing instability in soft materials under general loading conditions. *J Mech Phys Solids* 2021;151:104401.
- [74] Huang C, Wang Z, Quinn D, Suresh S, Hsia KJ. Differential growth and shape formation in plant organs. *Proc Natl Acad Sci* 2018;115(49):12359–64.
- [75] Li Z, Wang Q, Du P, Kadapa C, Hossain M, Wang J. Analytical study on growth-induced axisymmetric deformations and shape-control of circular hyperelastic plates. *Internat J Engng Sci* 2022;170:103594.
- [76] Wang F-F, Steigmann DJ, Dai H-H. On a uniformly-valid asymptotic plate theory. *Int J Non-Linear Mech* 2019;112:117–25.
- [77] Yu X, Fu Y, Dai H-H. A refined dynamic finite-strain shell theory for incompressible hyperelastic materials: equations and two-dimensional shell virtual work principle. *Proc R Soc Lond Ser A Math Phys Eng Sci* 2020;476(2237):20200031.
- [78] Bowden L, Byrne H, Maini P, Moulton D. A morphoelastic model for dermal wound closure. *Biomech Model Mechanobiol* 2016;15(3):663–81.
- [79] Liu Z, Swaddiwudhipong S, Hong W. Pattern formation in plants via instability theory of hydrogels. *Soft Matter* 2013;9(2):577–87.
- [80] Liu Y, Zhang H, Zheng Y, Zhang S, Chen B. A nonlinear finite element model for the stress analysis of soft solids with a growing mass. *Int J Solids Struct* 2014;51(17):2964–78.
- [81] Dervaux J, Ben Amar M. Localized growth of layered tissues. *IMA J Appl Math* 2010;75(4):571–80.

- [82] Haughton D, Orr A. On the eversion of compressible elastic cylinders. *Int J Solids Struct* 1997;34(15):1893–914.
- [83] Haughton D, Ogden R. Bifurcation of inflated circular cylinders of elastic material under axial loading—II. Exact theory for thick-walled tubes. *J Mech Phys Solids* 1979;27(5–6):489–512.
- [84] Saxena P. Finite deformations and incremental axisymmetric motions of a magnetoelastic tube. *Math Mech Solids* 2018;23(6):950–83.
- [85] Mehta S, Raju G, Kumar S, Saxena P. Instabilities in a compressible hyperelastic cylindrical channel due to internal pressure and external constraints. 2021, arXiv preprint [arXiv:2107.01375](https://arxiv.org/abs/2107.01375).
- [86] D'Errico J. `fminsearchbnd`, `fminsearchcon`, MATLAB central file exchange. 2021, <https://www.mathworks.com/matlabcentral/fileexchange/8277-fminsearchbnd-fminsearchcon>.